The Astrophysical Journal, 838:71 (21pp), 2017 March 20 https://doi.org/10.3847/1538-4357/aa64d0

Physical Properties of the Very Young PN Hen3-1357 (Stingray Nebula) Based on Multiwavelength Observations

Masaaki Otsuka[1], M. Parthasarathy[2], A. Tajitsu[3], and S. Hubrig[4]
[1] Institute of Astronomy and Astrophysics Academia Sinica, 11F of Astronomy-Mathematics Building, AS/NTU. No.1, Sec. 4, Roosevelt Road, Taipei 10617, Taiwan, R.O.C.; otsuka@asiaa.sinica.edu.tw (MO)
[2] Indian Institute of Astrophysics, II B lock Koramangala, Bangalore 560034, Karnataka, India
[3] Subaru Telescope, National Astronomical Observatory of Japan, 650 N Aohoku Place, Hilo, HI 96720, USA
[4] Leibniz-Institut fuer Astrophysik Potsdam (AIP) An der Sternwarte 12, D-14482 Potsdam, Germany
Received 2016 December 5; revised 2017 March 1; accepted 2017 March 3; published 2017 March 27

Abstract

We carried out a detailed analysis of the interesting and important very young planetary nebula (PN) Hen3-1357 (Stingray Nebula) based on a unique data set of optical to far-IR spectra and photometric images. We calculated the abundances of nine elements using collisionally excited lines (CELs) and recombination lines (RLs). The RL C/O ratio indicates that this PN is O-rich, which is also supported by the detection of the broad 9/18 μm bands from amorphous silicate grains. The observed elemental abundances can be explained by asymptotic giant branch (AGB) nucleosynthesis models for initially 1–1.5 $M_{\odot}$ stars with $Z = 0.008$. The Ne overabundance might be due to the enhancement of ^{22}Ne isotope in the He-rich intershell. Using the spectrum of the central star synthesized by Tlusty as the ionization/heating source of the PN, we constructed the self-consistent photoionization model with Cloudy to the observed quantities and derived the gas and dust masses, dust-to-gas mass ratio, and core mass of the central star. About 80% of the total dust mass is from warm–cold dust component beyond ionization front. Comparison with other Galactic PNe indicates that Hen3-1357 is an ordinary amorphous silicate-rich and O-rich gas PN. Among other studied PNe, IC4846 shows many similarities in properties of the PN to Hen3-1357, although their post-AGB evolution is quite different from each other. Further monitoring of observations and comparisons with other PNe such as IC4846 are necessary to understand the evolution of Hen3-1357.

Key words: dust, extinction – ISM: abundances – planetary nebulae: individual (Hen3-1357)

1. Introduction

Planetary nebula (PN) is the next evolutionary stage of asymptotic branch (AGB) stars. PNe consist of a dusty nebula and a hot central star that is evolving toward a white dwarf. So far, over 1000 PNe in the Galaxy have been identified (e.g., Frew 2008). Among PNe, Hen3-1357 (SAO244567, V839 Ara, PN G331.3-12.1, Stingray Nebula; Bobrowsky et al. 1998) has recently attracted much attention and has been studied actively since its first classification as a post-AGB star by Parthasarathy & Pottasch (1989).

Parthasarathy et al. (1993, 1995) discovered that Hen3-1357 has a young nebula and is going on post-AGB evolution; the UV spectrum of the 1988 study shows the P-Cygni profiles of the N V 1239/43 Å and C IV 1548/50 Å lines detected in the spectra, taken by the *International Ultraviolet Explore* (*IUE*), and the optical spectra from 1990 and 1992 show many nebular emission lines. Hen3-1357 is the first object evolving from a B1 type post-AGB supergiant into a PN within an extremely short timescale.

Using a distance of 5.6 kpc based on an extinction estimate from *UBV* photometry by Kozok (1985), Parthasarathy et al. (1993) estimated the luminosity of the central star to be 3000 $L_{\odot}$. Parthasarathy et al. (1995) found that the effective temperature ($T_{\rm eff}$) of the central star has increased from 37,500 K to 47,500 K during the same period. Later, Parthasarathy et al. (1997) estimated that $T_{\rm eff} = 50\,000$ K in 1995. A core mass versus luminosity relation suggests the core mass is 0.55 $M_{\odot}$, while the luminosity had faded by a factor of three in UV wavelength from 1988 to 1996 (Parthasarathy 2006). Increasing $T_{\rm eff}$ as the UV flux fades indicates a dropping luminosity, resulting that Hen3-1357 is rapidly evolving toward a white dwarf.

However, it is difficult to explain its evolution and evolutionary timescale. Parthasarathy et al. (1993) estimated a kinematical age to be ~2700 years by adopting the distance of 5.6 kpc, the (bright rim) radius of 0.″8 measured using the *Hubble Space Telescope* (*HST*) image (Bobrowsky 1994), and an expansion velocity of 8 km s^{-1} (Parthasarathy et al. 1993). According to the H-burning post-AGB evolution for initially 1.5 $M_{\odot}$ stars with metallicity $Z = 0.016$ (Vassiliadis & Wood 1994), such stars would take over 10^4 years to evolve into the white dwarf cooling track. The discrepancy between the observationally estimated and the model-predicted timescale suggests that Hen3-1357 might have experienced an extraordinary post-AGB evolution.

Reindl et al. (2014) demonstrated that Hen3-1357 has steadily increased its $T_{\rm eff}$ from 38,000 K in 1988 to a peak value of 60,000 K in 2002 and cooled again to 55,000 K in 2006 based on the stellar UV spectra. They proposed late He-flash evolution to explain this rapid $T_{\rm eff}$ increment. Reindl et al. (2017) found that $T_{\rm eff}$ further cooled down 50,000 K in 2015 using the newly obtained the *HST* UV spectra of the central star. Such a $T_{\rm eff}$ variation is found by Arkhipova et al. (2013), who estimated that $T_{\rm eff} = 57{,}000$ K in 1990, 55,000 K in 1992, and 41,000 K in 2011 using the [O III] 5007 Å line intensities relative to Hβ. Through a comparison with a theoretically calculated late thermal pulse (LTP) evolutionary path, Reindl et al. (2017) concluded that Hen3-1357 might have experienced an LTP. As Reindl et al. (2017) noted, however, any theoretical LTP model cannot yet fully reproduce the observed parameters of the central star of Hen3-1357.

Despite many efforts, the puzzling evolution of Hen3-1357 remains a fatal and challenging problem. For understanding Hen3-1357, properties of the nebula are crucial because the

Table 1
Observation log for Hen3-1357

Telescope/Instrument	Obs-Date
Spitzer/IRS	2005 Mar 20
MPG ESO 2.2 m/FEROS	2006 Apr 16
AKARI/IRC and FIS	2006 Dec 31
Spitzer/IRAC	2009 Apr 22

evolutionary history of the progenitor star has been imprinted in the nebula, as well. Utilizing nebular emission lines, one can easily derive elemental abundances such as C/N/O/Ne, which are essential key elements to prove AGB nucleosynthesis. The C/O ratio and the dust features seen in mid-IR spectra would suggest how much mass of the progenitor has gone into the formation of the nebula. It is of interest to investigate the conditions of the gas and dust and derive their masses in terms of material recycling in the Galaxy. Thus, nebula analysis is complementary for stellar analysis, and properties of the nebula can be the basis for understanding both the PN and its central star.

From these reasons, we investigated properties of the nebula based on a unique data set from UV to far-IR wavelengths (0.35–140 μm). This paper is organized as follows. In Section 2, we describe our optical high-dispersion spectroscopy using the Fiber-fed Extended Range Optical Spectrograph (FEROS; Kaufer et al. 1999) attached to the MPG ESO 2.2 m telescope and the archival mid-IR and far-IR data taken by the *AKARI* and *Spitzer* infrared space telescopes. In Section 3, we describe nebular abundance analysis. We first report the C/O and N/O ratios using the recombination lines of these elements in this PN. We compare the observed abundances with the AGB nucleosynthesis models to investigate the initial mass of the progenitor star. In Section 4, we construct the spectral energy distribution (SED) model using photoionization code Cloudy (Ferland et al. 2013, version C13.03) to investigate physical conditions of the nebula and the central star of PN (CSPN). We measure broadband magnitudes of the CSPN from the FEROS spectrum. We have a brief discussion on the CSPN's SED. In Section 5, we compare the observed elemental abundances and dust features with those of other PNe in order to verify Hen3-1357 as a PN. In Section 6, we summarize our work.

2. Observations and Data Reduction

We describe the photometric and spectroscopic data set taken by *Spitzer*, *AKARI*, and our FEROS observations. The observation log is summarized in Table 1. The *AKARI* data were obtained in 2006 May 6–2007 August 28, the middle date is around 2006 December 31.

2.1. Spitzer and AKARI Photometry

We measured the mid-IR flux densities for Bands 1-4 of the *Spitzer*/Infrared Array Camera (IRAC; Fazio et al. 2004), where the central wavelengths (λ_c) are 3.6, 4.5, 5.8, and 8.0 μm, respectively. We reduced the basic calibrated data (BCD, program ID: 50116, obs AORKEY: 25445376, PI: G. Fazio) using mosaicking and point-source extraction software (MOPEX)[5] provided by the Spitzer Science Center (SSC) to create a mosaic image for each band. We subtracted artificial features seen in the images as best as possible. After we subtracted out surrounding stars by point-spread function fittings using the DIGIPHOT photometry package in IRAF v.2.16,[6] we performed aperture photometry. The results are summarized in Table 2.

To trace the amorphous silicate feature seen in the *Spitzer*/IRS spectrum, we used the *AKARI* Infrared Camera (IRC; Onaka et al. 2007) S9W ($\lambda_c = 9\,\mu$m) and L18W ($\lambda_c = 18\,\mu$m). We used the *AKARI* Far-Infrared Surveyor (FIS; Kawada et al. 2007) data as vital constraints to the warm–cold dust continuum in the SED modeling. For this end, we utilized the photometry measurements by Yamamura et al. (2010) for the IRC two bands and FIS Bright Source Catalog Ver.2 for the FIS-N60, WIDE-S, and WIDE-L bands at $\lambda_c = 65$, 90, and 140 μm, respectively. These data were taken by the *AKARI* all-sky survey. We list these flux densities in Table 2, where $A(-B)$ means $A \times 10^{-B}$ hereafter.

2.2. MPG ESO 2.2 m FEROS Spectroscopy

We secured the optical high-dispersion spectrum (3500–9200 Å) using the FEROS attached to the MPG ESO 2.2 m Telescope, La Silla, Chile (Prop.ID: 77.D-0478A, PI: M. Parthasarathy).

The weather condition was stable and clear throughout the night, and the seeing was 0.″8–1.″17 (average: 0.″97) measured from the differential image motion monitor. FEROS's fibers use 2.″0 apertures and provide simultaneously the object and sky spectra. The detector is the EEV CCD chip with 2048 × 4096 pixels of 15 × 15 μm square. We selected a 1 × 1 on-chip binning and low gain mode.[7] The atmospheric dispersion corrector (ADC) was not used during the observation. The exposure time was a single 2100 sec at an airmass of 1.297–1.380. For the flux calibration and blaze function correction, we observed the standard star HR 3454 (Hamuy et al. 1992, 1994) at airmass ∼1.2. Since we did not use the ADC, a color-dependent displacement of the source from differential atmospheric refraction (DAR) might be present. However, we took the data of the Stingray nebula and HR 3454 to be at a similar airmass. Therefore, we believe that the DAR effect on the inferred extinction coefficients, the derived electron temperatures, and therefore on the derived ionic and elemental abundances would be largely reduced. We reduced the data with the echelle spectra reduction package ECHELLE in IRAF using a standard reduction manner including bias subtraction, removing scattered light, detector sensitivity correction, removing cosmic-ray hits, airmass extinction correction, flux-density calibration, and an all echelle order connection. Using the sky spectrum, we subtracted the sky lines from the Hen3-1357 spectrum. The average resolving power ($\lambda/\Delta\lambda$) is 44,950, which was measured from the average full width at half maximum (FWHM) of over 300 Th–Ar comparison lines obtained for the wavelength calibrations. The signal-to-noise ratios per pixel were ∼2–12 for the continuum.

[5] http://irsa.ipac.caltech.edu/data/SPITZER/docs/dataanalysistools/tools/mopex/

[6] IRAF is distributed by the National Optical Astronomy Observatories, operated by the Association of Universities for Research in Astronomy (AURA), Inc., under a cooperative agreement with the National Science Foundation. http://iraf.noao.edu.

[7] We measured the gain = 4.99 e^- ADU^{-1} and readout-noise = 8.31 e^- using the IRAF task FINDGAIN.

Table 2
Near- to Far-IR-Band Flux Densities of Hen3-1357

λ_c (μm)	Tele/Instr/Band	F_ν (mJy)	F_λ (erg s^{-1} cm^{-2} μm^{-1})
3.6	*Spitzer*/IRAC/Band1	1.09(+1) ± 5.22(−1)	2.58(−12) ± 1.24(−13)
4.5	*Spitzer*/IRAC/Band2	1.61(+1) ± 5.02(−2)	2.38(−12) ± 7.42(−15)
5.8	*Spitzer*/IRAC/Band3	1.08(+1) ± 1.68(−1)	9.87(−13) ± 1.53(−14)
8.0	*Spitzer*/IRAC/Band4	3.97(+1) ± 8.20(−1)	1.89(−12) ± 3.91(−14)
9.0	*AKARI*/IRC/S9W	8.87(+1) ± 8.62(0)	3.13(−12) ± 3.04(−13)
65.0	*AKARI*/FIS/N60	2.25(+3) ± 3.52(+2)	1.60(−12) ± 2.50(−13)
90.0	*AKARI*/FIS/WIDE-S	1.88(+3) ± 5.06(+1)	6.98(−13) ± 1.87(−14)
140.0	*AKARI*/FIS/WIDE-L	3.77(+2) ± 2.75(+2)	5.77(−14) ± 4.21(−14)

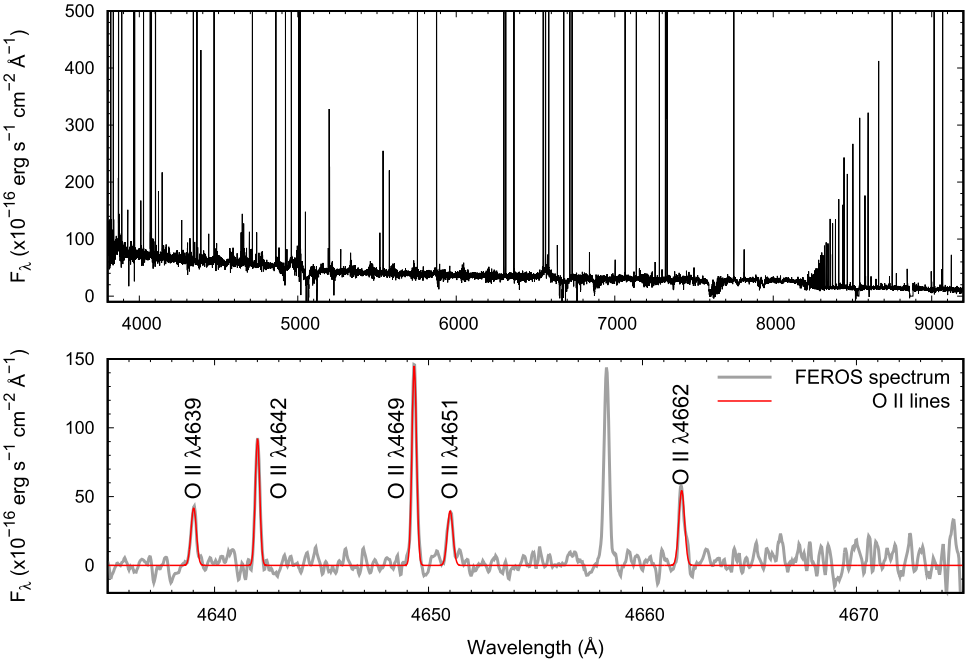

Figure 1. (Upper panel) FEROS spectrum of Hen3-1357 in the range between 3800 Å and 9200 Å. (Lower panel) FEROS spectrum in 4635-4675 Å (gray line) and the Gaussian fitting results for the O II lines in this wavelength range (red line). The local continuum was subtracted out.

The resultant FEROS spectrum is presented in Figure 1; the detected recombination lines (RLs) of O II are shown in the lower panel. As far as we know, the N and O RLs such as N II and O II are detected in this PN for the first time.

2.3. Spitzer/IRS Spectrum

To investigate dust features and perform plasma diagnostics using fine-structure lines, we analyzed the mid-IR spectra taken by the *Spitzer*/Infrared Spectrograph (IRS; Houck et al. 2004) with the Short-Low (SL, 5.2–14.5 μm, the slit dimension: $\sim$3.″6 × 57″), Short-High (SH, 9.9–19.6 μm, 4.″7 × 11.″3), and Long-High modules (LH, 18.7–37.2 μm, 11.″1 × 22.″3).

We processed the BCD (program ID: 3633, obs AORKEY: 11312640, PI: B. Matthew) using the data reduction packages SMART v.8.2.9 (Higdon et al. 2004) and IRSCLEAN v.2.1.1[8] provided by the SSC. We scaled the flux density of the reduced LH spectrum to match with that of the reduced SH spectrum in the overlapping wavelength and we obtained the single 9.9–37.2 μm spectrum. Then, using a similar method, we combined this high-dispersion spectrum and the SL 5.2–14.5 μm spectrum into the single 5.2–37.2 μm spectrum.

We present the resultant spectrum in Figure 2. The intensity peak positions of the identified atomic lines are marked by the vertical lines. We detected Ne, S, and Ar fine-structure lines. The spectrum clearly shows two broad features (indicated by the horizontal red lines) attributed to amorphous silicate grains; the features centered at 9 μm and 18 μm are due to the Si-O stretching mode and the O-Si-O bending mode, respectively. Perea-Calderón et al. (2009) reported that this PN is an O-rich dust object. We did not identify any carbon-based dust grains and molecules in the *Spitzer*/IRS spectrum. Thus, we can conclude that Hen3-1357 has an O-rich dust nebula.

3. Results

3.1. Scaling the Flux Density of the Spitzer/IRS Spectrum

We performed a correction to recover the loss of light from Hen3-1357 by the slit.

First, using the *AKARI*/IRC 9.0 μm band photometry listed in Table 2, we scaled the flux density of the spectrum by considering the *AKARI*/IRC 9.0 μm filter transmission curve by a constant scaling factor of 0.951. Next, using this scaled

[8] http://irsa.ipac.caltech.edu/data/SPITZER/docs/dataanalysistools/tools/irsclean/

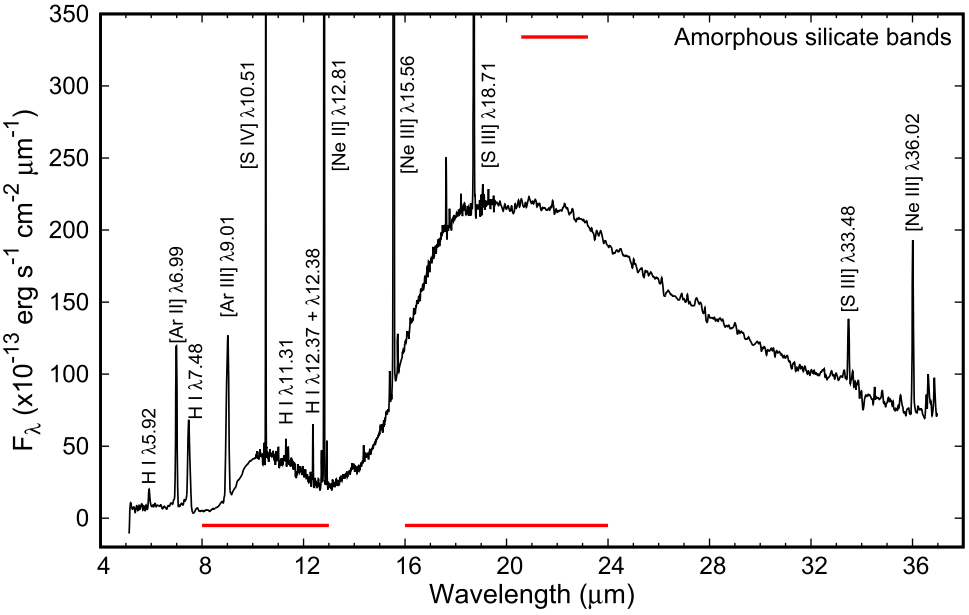

Figure 2. *Spitzer*/IRS spectrum of Hen3-1357. The identified atomic lines and amorphous silicate features are denoted.

spectrum and the *Spitzer*/IRAC 8.0 μm filter transmission curve, we measured the *Spitzer*/IRAC 8.0 μm band flux density. The measured value 1.90(−12) erg s^{-1} cm^{-2} μm^{-1}is consistent with the IRAC 8.0 μm photometry result.

AKARI/IRC 9.0 μm and *Spitzer*/IRAC 8.0 μm bands include atomic lines of H, Ne, S, and Ar certainly contributing to these two bands. As noted in Section 3.4, we did not find a significant difference between optical nebular line intensities relative to the Hβ measured in 2006 and in 2011. This means that the ionization and elemental abundances of the nebula might not have changed between 2006 and 2011.

Our adopted scaling factor (0.951) indicates that the IR-band flux decreased by ∼5% between 2005 and 2009. Therefore, we assume that the mid-IR wavelength evolution had not dramatically changed between 2005 and 2009.

Taking into account these analyses, we scaled the flux density of the spectrum to match the *AKARI*/IRC 9.0 μm band flux density.

3.2. The Hβ Flux of the Entire Nebula

The Hβ flux of the entire nebula is necessary for setting the nebula's hydrogen density structure in our SED modeling as well as for calculating the $Ne^{+,2+}$, $S^{2+,3+}$, and $Ar^{+,2+}$ to H^+ number density ratios and electron density n_e and temperature T_e using mid-IR fine-structure lines of these ions.

Since the H I 7.46 μm line is in the longer wavelength edge of the SL2 spectrum (5.13–7.60 μm) and also in the shorter edge of the SL1 spectrum (7.46–14.29 μm), we did not employ this line for estimating the Hβ line flux of the entire nebula. Therefore, we obtained the Hβ line flux by utilizing the theoretical H I $I(n = 7–6$ and $11–8)/I(n = 4–2)$ intensity ratio calculated by Storey & Hummer (1995), where n is the principal quantum number. Note that a detected line at 12.37 μm (see Figure 2) indeed is composed of H I $n = 7–6$ at 12.37 μm and $n = 11–8$ at 12.38 μm. From the I(12.37 μm + 12.38 μm)/I(Hβ) = 1.04(−2) in the case of an $n_e = 10^4$ cm^{-3} and a $T_e = 10^4$ K (Storey & Hummer 1995), we estimated the Hβ flux of the entire nebula to be 9.83 (−12) ± 7.33(−13) erg s^{-1} cm^{-2}.

Table 3
Derived c(Hβ) Ratios

$\lambda_{lab.}$ (Å)	Line	c(Hβ)
3797.9	B10	8.25(−2) ± 6.43(−3)
3835.4	B9	3.25(−2) ± 5.17(−3)
3970.1	B7	7.39(−2) ± 2.95(−3)
4101.7	B6	4.38(−1) ± 3.56(−3)
4340.5	B5	1.34(−1) ± 5.16(−3)
8545.4	P15	2.03(−2) ± 1.04(−2)
8598.4	P14	3.84(−2) ± 2.54(−3)
8665.0	P13	7.49(−2) ± 2.48(−3)
8750.5	P12	6.64(−2) ± 1.98(−3)
9014.9	P10	1.18(−2) ± 2.25(−3)

Note. For the interstellar reddening correction to the FEROS spectrum, we adopted the average c(Hβ) = 8.27(−2) ± 3.47(−2).

3.3. Flux Measurements

We measured the fluxes of the emission lines by Gaussian fittings and then corrected these fluxes using the formula

$$I(\lambda) = F(\lambda) \cdot 10^{c(\mathrm{H}\beta)(1+f(\lambda))}, \quad (1)$$

where $I(\lambda)$ is the de-reddened line flux, $F(\lambda)$ is the observed line flux, $f(\lambda)$ is the interstellar extinction function at λ computed by the reddening law of Cardelli et al. (1989) with $R_V = 3.1$, and c(Hβ) is the reddening coefficient at Hβ.

We measured c(Hβ) values by comparing the observed 10 Balmer and Paschen line ratios to Hβ with the theoretical ratios of Storey & Hummer (1995) for a $T_e = 10^4$ K and an $n_e = 10^4$ cm^{-3} under the Case B assumption. To reduce the c(Hβ) estimation errors originated from the H I absorptions in the flux standard star HR 3454, we estimated c(Hβ) using different line ratios. The derived c(Hβ) values are listed in Table 3. Since the Hα line was saturated, we did not calculate c(Hβ) using the F(Hα)/F(Hβ) ratio. Finally, we adopted the average c(Hβ) = 8.27(−2) ± 3.47 (−2). The scatter between the estimated c(Hβ) could be due to the H I absorptions' depth of HR 3454 measured by Hamuy et al. (1992, 1994). We did not correct interstellar extinction for the

Spitzer/IRS spectrum because the extinction is negligibly small in the mid-IR wavelength.

For the year 2006, Reindl et al. (2014) reported $E(B-V) = 0.11$, corresponding to $c(\mathrm{H}\beta) = 0.16$. Although they did not give the uncertainty of $E(B-V)$, we assume $\delta E(B-V) = 0.02$ from the fact that they measured $E(B-V) = 0.14 \pm 0.02$ in the year 1997. Thus, their $c(\mathrm{H}\beta)$ for the year 2006 is estimated to be 0.16 ± 0.03, which is consistent with ours.

In Table 13, we list 180 nebular lines detected in the FEROS spectrum. Since the [O III] 5007 Å and Hα lines were saturated, we do not list their fluxes. We calculated the average heliocentric radial velocity 12.30 km s^{-1} and local standard of rest (LSR) radial velocity 12.29 km s^{-1} using all the identified lines in the FEROS spectrum (1σ uncertainty is 0.25 km s^{-1}). Our heliocentric radial velocity is in good agreement with Arkhipova et al. (2013, 12.6 ± 1.7 km s^{-1}).

In Table 14, we listed the fluxes of the identified 14 atomic gas emission lines detected in the flux-density scaled *Spitzer*/IRS spectrum, where the fluxes are normalized with respect to the Hβ flux of the entire nebula.

3.4. Comparison of Line Fluxes Between 2006 and 2011

We investigated the possibility of temporal variations of the emission-line intensities by comparing our measurements with those of Arkhipova et al. (2013), who obtained the 3500–7200 Å low-resolution spectrum (FWHM = 4.5 Å) on 2011 June at the South African Astronomical Observatory (SAAO). In Table 15, we list their measured line intensities that overlapped with ours. In 2006–2011, the nebular line fluxes did not significantly change. Indeed, the $I(\lambda)$ in 2006 are very similar to those in 2011 ($I(2011)/I(2006) = 1.11 \pm 0.02$, correlation factor of 0.995). Thus, the ionization and elemental abundances of the nebula might not be largely changed in 2006–2011. Variation in the $T_{\rm eff}$ of the central star by 5000 K to 10,000 K in a 5- to 10-year interval might not immediately change the nebular morphology, parameters, and abundances in the same time period.

3.5. Plasma Diagnostics

In forbidden line analysis, we employed the NEBULAR package by Shaw & Dufour (1995) and in recombination line analysis, we used private software. In both emission-line analyses, we adopted effective recombination coefficients, transition probabilities, and effective collision strengths listed in Otsuka et al. (2010, their Table 7).

We performed plasma diagnostics using collisionally excited lines (CELs) and RLs. We greatly increased the results compared to Parthasarathy et al. (1993), who obtained one $n_{\rm e}$ and two $T_{\rm e}$ using the optical spectrum taken in 1992, and Arkhipova et al. (2013), who deduced one $n_{\rm e}$ and four $T_{\rm e}$ based on the 3500–7200 Å spectrum taken in 2011. In Table 4, we list the diagnostic line ratios to derive $n_{\rm e}$ and $T_{\rm e}$ and the resultant values. In Figure 3, we present the $n_{\rm e}$–$T_{\rm e}$ diagram using the diagnostic CEL ratios. "opt" indicates the result from the optical forbidden line ratio; e.g., [S III] $I(9069\,\text{Å})/I(6312\,\text{Å})$ ratio. "ir/opt" means the result from the mid-IR fine-structure lines and optical forbidden line; e.g., [S III] $I(18.7/33.5\,\mu\text{m})/I(9067\,\text{Å})$ ratio. We note that CEL emissivities are in general sensitive to $n_{\rm e}$ and $T_{\rm e}$, accordingly, CEL ionic abundances depend on a selection of $n_{\rm e}$ and $T_{\rm e}$.

First, we calculated $n_{\rm e}$ using CELs. The $n_{\rm e}$–$T_{\rm e}$ diagram indicates that the average $n_{\rm e}$ is in the range from $\sim$2000 cm^{-3} in neutral gas regions (by the $n_{\rm e}$([N I]) curve, ID(1)) and $\sim$20,000 cm^{-3} in highly ionized gas regions (by the $n_{\rm e}$([Ar IV]) curve, ID(7)) and the average $T_{\rm e}$ is $\sim$8000–10,000 K. We derived all $n_{\rm e}$ by adopting a constant $T_{\rm e} = 9000$ K.

Next, we calculated $T_{\rm e}$([O I]) by adopting $n_{\rm e}$([N I]), $T_{\rm e}$([Ar III]) by the average $n_{\rm e} = 22{,}980$ cm^{-3} between $n_{\rm e}$([S III]) and $n_{\rm e}$([Cl III]), $T_{\rm e}$([S III]) by $n_{\rm e}$([S III]), $T_{\rm e}$([Cl III]) by $n_{\rm e}$([Cl III]), and both $T_{\rm e}$([O III]) and $T_{\rm e}$([Ne III]) by adopting $n_{\rm e}$([Ne III]), respectively.

To obtain $T_{\rm e}$([O II]), $n_{\rm e}$([O II], and $T_{\rm e}$([N II]), which are representative $n_{\rm e}$ and $T_{\rm e}$ in lower ionization regions, we subtracted respective contributions from O^{2+} and N^{2+} recombination to the [O II] 7320/30 Å lines and the [N II] 5755 Å line. We calculated the contributions to these lines, $I_{\rm R}$([O II] 7320/30 Å) and $I_{\rm R}$([N II] 5755 Å), using the following equations from Liu et al. (2000):

$$\frac{I_{\rm R}(\text{[O II] 7320/30 Å})}{I(\mathrm{H}\beta)} = 9.36\left(\frac{T_{\rm e}}{10^4}\right)^{0.44}\frac{n(\mathrm{O}^{2+})}{n(\mathrm{H}^{+})}, \quad (2)$$

$$\frac{I_{\rm R}(\text{[N II] 5755 Å})}{I(\mathrm{H}\beta)} = 3.19\left(\frac{T_{\rm e}}{10^4}\right)^{0.33}\frac{n(\mathrm{N}^{2+})}{n(\mathrm{H}^{+})}. \quad (3)$$

Here, $n(O^{2+})/n(H^{+})$ and $n(N^{2+})/n(H^{+})$ are the number density ratios of the O^2 and N^{+} with respect to the H^{+}, respectively.

We adopted the CEL $O^{2+} = 1.87(-4) \pm 1.39(-6)$ (see Section 3.6) in order to obtain the $I_{\rm R}$([O II] 7320/30 Å) = 0.16 ± 0.01, where $I(\mathrm{H}\beta) = 100$. Based on the result that the CEL O^{2+} is consistent with the RL O^{2+}, we assumed that the CEL N^{2+} could be very close to the RL N^{2+}. Here, we adopted the RL $N^{2+} = 6.97(-5) \pm 3.17(-5)$ (see Section 3.6) to calculate the $I_{\rm R}$([N II] 5755 Å) of 0.33 ± 0.05.

The [O II] $I(3726\,\text{Å})/I(3729\,\text{Å})$ ratio is an $n_{\rm e}$ indicator and the $I(3726/29\,\text{Å})/I(7320/30\,\text{Å})$ ratio is sensitive to both $T_{\rm e}$ and $n_{\rm e}$. In Hen3-1357, $n_{\rm e}$ exceeds the critical density of the [O II] 3726/29 Å lines, so the $I(3726\,\text{Å})/I(3729\,\text{Å})$ ratio could not give reliable $n_{\rm e}$. Therefore, we used the $I(3726/29\,\text{Å})/I(7320/30\,\text{Å})$ ratio to derive an $n_{\rm e}$ required for the N^{+}, O^{+}, Cl^{+}, Ar^{+}, and Fe^{2+} calculations. We obtained $n_{\rm e}$([O II]) by adopting a constant $T_{\rm e} = 9000$ K and then obtained $T_{\rm e}$([N II]) using $n_{\rm e}$([O II]) = 17,520 cm^{-3}.

We found the discrepancy between two $T_{\rm e}$([S III]) values (IDs 10 and 11). This might be due to the underestimated [S III] 9069 Å that appeared in the red wavelength edge of the FEROS spectrum because the ionic S^{2+} abundance from this line is $\sim$14% smaller than that from the fine-structure [S III] lines, which are insensitive to $T_{\rm e}$ (see Table 5). As we explained in Section, 2.2, the differential atmospheric refraction (DAR) effect might have affected [S III] 9069 Å, although we cannot exactly estimate how much light was lost from the [S III] 9069 Å line. The DAR effect might affect widely separated diagnostic line intensity ratios. However, for the S^{2+} abundance estimate, we adopted the average $T_{\rm e}$ between two $T_{\rm e}$([S III]), thus, reducing the effects by inconsistency between these two $T_{\rm e}$([S III]).

Similarly, if we underestimate the [O II] 7320/30 Å intensity by $\sim$14%, which is an expected value from the above analysis for the S^{2+} abundance, we obtain $n_{\rm e}$([O II]) = 20 300 cm^{-3}. Then, using $n_{\rm e}$([O II]), we obtain $T_{\rm e}$([N II]) = 9010 K. Under $n_{\rm e}$([O II]) and $T_{\rm e}$([N II]), the N^{+}, O^{+}, Cl^{+}, and Fe^{2+} abundances[9] would increase by $\sim$12%. Even if the DAR effect is

[9] We calculated these ionic abundances under $n_{\rm e}$([O II]) and $T_{\rm e}$([N II]) (see Table 16).

Table 4
Summary of Plasma Diagnostics

n_e-derivations (this work for the year 2006)					Arkhipova et al. (2013)
ID	Ion	Diagnostic line ratio	Ratio	Result (cm^{-3})	(cm^{-3})
(1)	[N I]	I(5197 Å)/I(5200 Å)	1.59(0) ± 3.16(−2)	1390 ± 90	···
(2)	[S II]	I(6716 Å)/I(6731 Å)	3.23(−1) ± 7.30(−2)	5710 ± 1790	8740 ± 7701
(3)	[O II]	I(3726/29 Å)/I(7320/30 Å)	4.37(0) ± 1.17(−1)	17,520 ± 530	···
(4)	[S III]	I(18.7 μm)/I(33.5 μm)	3.94(0) ± 3.32(−1)	21,990 ± 4840	···
(5)	[Cl III]	I(5517 Å)/I(5537 Å)	4.86(−1) ± 1.69(−2)	23,970 ± 3120	···
(6)	[Ne III]	I(15.6 μm)/I(36.0 μm)	1.56(+1) ± 9.67(−1)	22,750 ± 5850	···
(7)	[Ar IV]	I(4711 Å)/I(4740 Å)	4.88(−1) ± 4.55(−2)	22,720 ± 4360	···
	H I	Paschen decrement		10,000 – 20,000	···
T_e-derivations (this work for the year 2006)					Arkhipova et al. (2013)
ID	Ion	Diagnostic line ratio	Ratio	Result (K)	(K)
(8)	[O I]	I(6300/63 Å)/I(5577 Å)	9.69(+1) ± 2.57(0)	8470 ± 70	···
(9)	[N II]	I(6548/83 Å)/I(5755 Å)	6.38(+1) ± 1.55(0)	9280 ± 100	11,066 ± 1752
(10)	[S III]	I(9069 Å)/I(6312 Å)	1.22(+1) ± 6.34(−1)	8880 ± 180	11,831 ± 2286
(11)	[S III]	I(18.7/33.5 μm)/I(9069 Å)	1.38(0) ± 7.82(−2)	7430 ± 280	···
(12)	[Cl III]	I(5517/37 Å)/I(8434/8501 Å)	2.03(+1) ± 4.54(0)	7490 ± 850	···
(13)	[Ar III]	I(7135/7751 Å)/I(5191 Å)	2.09(+2) ± 1.14(+1)	8670 ± 150	···
(14)	[Ar III]	I(9.01 μm)/I(7135/7751 Å)	9.70(−1) ± 4.27(−2)	8400 ± 310	···
(15)	[O III]	I(4959 Å)/I(4363 Å)	5.91(+1) ± 7.27(−1)	9420 ± 40	11,553 ± 1579
(16)	[Ne III]	I(15.6 μm)/I(3869/3968 Å)	1.92(0) ± 7.34(−2)	8560 ± 70	···
T_e(PJ)		(I_λ(8194 Å)-I_λ(8169 Å))/I(P11)	2.16(−2) ± 2.53(−3)	8090 ± 1680	···
T_e(He I)	He I	I(7281 Å)/I(6678 Å)	1.83(−1) ± 7.38(−3)	8340 ± 330	···
T_e(He I)	He I	I(7281 Å)/I(5876 Å)	4.95(−2) ± 1.80(−3)	7980 ± 360	···

Note. For a comparison, the results from Arkhipova et al. (2013, for the year 2011) are listed in the last column.

present in our FEROS spectrum, the potential error of $c(H\beta)$, T_e and n_e, and ionic/elemental abundances caused by the DAR effect would be ∼15% or less. Hence, our conclusion on these physical parameters derived from the CELs and the RLs does not change.

Finally, we calculated T_e and n_e using He I lines and H I Paschen series. We calculated T_e(He I) using He I I(7281 Å)/I(6678 Å) and I(7281 Å)/I(5876 Å) ratios using the recombination coefficients in a constant $n_e = 10^4\,cm^{-3}$ provided by Benjamin et al. (1999). We calculated the Paschen jump T_e(PJ) using Equation (7) of Fang & Liu (2011). The H I P11 line is in an echelle order gap. Therefore, we obtained the *expected I* (P11) using the observed H I P12 line and the theoretical I(P11)/I(P12) ratio of 1.30 in $n_e \sim 10^2$–$10^5\,cm^{-3}$ and $T_e \sim$ 5000–15,000 K (Storey & Hummer 1995). Thus, we obtained n_e ∼10,000–20,000 cm^{-3} by comparing the observed I(Pn)/I(P10) ratios (n is from 12 to 42) and the theoretical calculations under the Case B assumption and T_e(PJ) = 8090 K by Storey & Hummer (1995).

As a comparison, the results from Arkhipova et al. (2013, for the year 2011) are listed in the last column. Arkhipova et al. (2013) reported T_e([O III]) = 11,553 ± 1579 K, T_e([O II]) = 11,983 ± 770 K,[10] T_e([N II]) = 11,066 ± 1752 K, T_e([S III]) = 11,831 ± 2286 K,[11] and n_e([S II]) = 8740 ± 7701 cm^{-3}. The difference between their T_e([O III]) and ours is due to the [O III] 4363 Å intensity (see Table 15). Under a constant n_e, the T_e([O III]) becomes higher as the [O III] I(4959/5007 Å)/I(4363 Å) ratio becomes lower. The [N II] n_e–T_e curve in Figure 3 suggests that the discrepancy in T_e([N II]) could be due to the difference in adopted n_e.

[10] However, the auroral [O II] lines are out of their spectrum taken in 2011.
[11] The nebular [S III] lines are out of their spectrum, too.

3.6. Ionic Abundance Derivations

In Table 16, we list n_e and T_e adopted for calculating each ionic abundance. We determined these values by referring to the n_e–T_e diagram and taking the ionization potential (IP) of the targeting ion into account. We calculated the CEL ionic abundances by solving an equation of population at multiple energy levels (from two energy levels for Ne^+ and Ar^+ and 33 levels for Fe^{2+}) under the listed n_e and T_e. We adopted a constant $n_e = 10^4\,cm^{-3}$ and the average T_e(He I) = 8160 K to calculate He^+. For the RL C^{2+}, N^{2+}, and O^{2+}, we adopted $n_e = 10^4\,cm^{-3}$ and T_e(PJ).

We summarize the resultant CEL and RL ionic abundances in Tables 5 and 6, respectively. When we detected two or more lines of a target ion, we derived each ionic abundance using each line intensity. Then, we adopted the weight-average value as the representative ionic abundance as listed in the last line of each ion by boldface. We give the 1σ uncertainty of each ionic abundance, which accounts for the uncertainties of line fluxes (including $c(H\beta)$ uncertainty), T_e, and n_e.

The CEL abundances calculated using the optical lines are well consistent with ones using mid-IR fine-structure lines, indicating that the calculated CEL ionic abundances are the result of the proper selection of T_e, in particular, and of accurate scaling flux of the *Spitzer*/IRS spectrum.

We obtained the RL N^{2+} and O^{2+} in this PN for the first time. The higher multiplet lines are in general insensitive to Case A or Case B assumptions and reliable because these lines are less affected by both resonance fluorescence by starlight

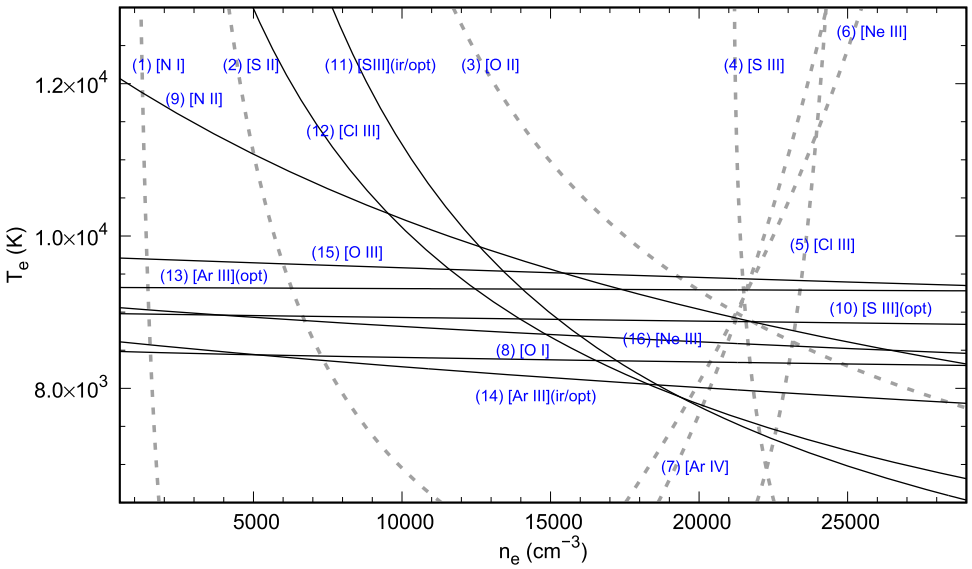

Figure 3. n_e–T_e diagram based on CEL diagnostic line ratios. The dashed and thick lines with "(ID)" indicate the n_e- and T_e-diagnostic curves generated by the line ratios listed in Table 4, respectively.

and recombination from higher terms. The consistency between the RL C^{2+} abundance by the multiple V6 4267.18 Å line and by the V2 6578.05 Å line indicates that the RL C^{2+} from both lines can be reliable. We can have the similar conclusion for the RL O^{2+} and N^{2+} abundances. The RL O^{2+} abundances are well consistent among the O II V1 4638/42/49/51/62/76 Å, V2 4349/67 Å, V10 4069.6/69.9/72/76 Å, V19 4153 Å, and V20 4105 Å lines. The RL N^{2+} abundances are derived using the V3 5679 Å and 4631 Å lines.

As is compared in Table 7, our ionic abundances agree with Arkhipova et al. (2013). However, we found obvious discrepancies in Ne^{2+} and S^{2+}. Their S^{2+} seems to be derived using the auroral line [S III] 6312 Å. Although they did not report the detection of any [Ne III] lines in their spectrum taken in 2011, we assume that they derived the Ne^{2+} using nebular [Ne III] lines. The Ne^{2+} and S^{2+} differences between Arkhipova et al. (2013) and us are due to the adopted T_e. We stress that our adopted T_e for the Ne^{2+} and S^{2+} is determined using the [Ne III] and [S III] fine-structure, nebular, and auroral lines. For instance, if we adopt their T_e([O III]) = 11,553 K to calculate the Ne^{2+} using the nebular [Ne III] lines, the volume emissivities of these [Ne III] lines become 2.66 times higher than those in our adopted T_e = 8560 K. Accordingly, the Ne^{2+} is down to 3.18(−5), which is consistent with Arkhipova et al. (2013). However, since the emissivities of the fine-structure [Ne III] lines do not largely change, even in both 8560 K by ours and 11,553 K by Arkhipova et al. (2013), the Ne^{2+} abundances using the fine-structure [Ne III] lines keep 8.38 (−5) (from the [Ne III] 15.56 μm line) and 8.57(−5) (from the [Ne III] 36.02 μm line). That is, we find out the *spurious* Ne^{2+} derivation discrepancy between the nebular and the fine-structure lines. We confirmed that a similar conclusion can apply for S^{2+}. Thus, if the nebula condition is in a steady state and had not dramatically changed between 2006 and 2011, we can conclude that our Ne^{2+} and S^{2+} are more reliable.

3.7. Elemental Abundance Derivations Using the ICFs

By introducing the ionization correction factor (ICF), we inferred the nebular abundances from their ionic abundances. We calculated these ICF(X) derived based on the fraction of the observed ionic abundances with similar ionization potentials to the target element. The ICF(X) of element X is listed in the last line of each element of Tables 5 and 6. The abundance of the element X $n(X)/n(H)$ corresponds to the value derived from the ICF(X) $\cdot \Sigma_{m=1} n(X^{m+})/n(H^+)$. We will compare these ICF(X) based on IPs with those calculated by Cloudy photoionization model later.

As shown in Section 3.6, we obtained the O(CEL), Ne, S, and Ar ionic abundances in various ionization stages. Thus, for these elements, we can adopt ICF(X) = 1.0. We adopted ICF (He) = 1.0 because we did not detect the nebular He II lines. Assuming that N corresponds to the sum of the N^+ and N^{2+}, we recovered the unobserved N^{2+}(CEL) using the ICF(N) proposed by Delgado-Inglada et al. (2014). Then, using ICF(N) for N (CEL), we determined ICF(N(RL)). Since the IPs in both C and N ions are similar, we assumed that ICF(C(RL)) is as same as ICF(N (RL)). ICF(O(RL)) corresponds to O(CEL)/O^{2+}(CEL). ICF(Cl) corresponds to the $Ar/(Ar^+ + Ar^{2+})$ ratio. For ICF(Fe), we adopted Equation (3) of Delgado-Inglada & Rodríguez (2014).

In Table 8, we summarize the resultant elemental abundances derived by introducing the ICFs. The value ϵ(X) in the third column is $12 + \log_{10} n(X)/n(H)$. The value in the last column is the relative abundance to the Sun. We referred to the solar abundance by Asplund et al. (2009). Our work improved nebular elemental abundances calculated by the pioneering work of Parthasarathy et al. (1993) and a recent comprehensive study of Arkhipova et al. (2013).

Using the RL C, N, and O, we derived the C/O and the N/O ratios using the same type of emission lines, i.e., RLs. These ratios are important proofs of the initial mass of the central star. In Table 8, we list an *expected* C(CEL) based on the assumption that the RL C/O ratio (0.21 ± 0.09) is consistent with the CEL C/O ratio.

The RL C/O ratio indicates that Hen3-1357 is an O-rich PN, which is also supported by the detection of the amorphous silicate features. The average of the logarithmic difference between the nebular and solar abundances of S, Cl, and Ar $\langle$[S, Cl, Ar/H]$\rangle$ = −0.21 ± 0.10 indicates that this PN is about a half of a solar

Table 5
The Ionic Abundances Derived Using CELs

Elem. (X) (1)	Ion (X^{m+}) (2)	$\lambda_{lab.}$ (3)	$I(\lambda)$ ($I(H\beta) = 100$) (4)	$n(X^{m+})/n(H^+)$ (5)	Elem. (X) (6)	Ion (X^{m+}) (7)	$\lambda_{lab.}$ (8)	$I(\lambda)$ ($I(H\beta) = 100$) (9)	$n(X^{m+})/n(H^+)$ (10)
N(CEL)	N^0	5197.90 Å	3.63(−1) ± 4.38(−3)	1.11(−6) ± 3.46(−8)	S	S^+	4068.60 Å	4.47(0) ± 8.61(−2)	1.13(−6) ± 1.37(−7)
		5200.26 Å	2.28(−1) ± 3.59(−3)	1.07(−6) ± 1.82(−8)			4076.35 Å	1.51(0) ± 2.90(−2)	1.17(−6) ± 1.43(−7)
			Average	**1.09(−6) ± 2.83(−8)**			6716.44 Å	6.07(0) ± 1.54(−1)	9.55(−7) ± 1.57(−7)
	N^+	5754.64 Å	2.55(0) ± 3.87(−2)	3.61(−5) ± 2.41(−6)			6730.81 Å	1.25(+1) ± 3.19(−1)	1.07(−6) ± 1.13(−7)
		6548.04 Å	4.10(+1) ± 9.67(−1)	3.60(−5) ± 1.24(−6)				**Average**	**1.06(−6) ± 1.30(−7)**
		6583.46 Å	1.21(+2) ± 2.91(0)	3.60(−5) ± 1.25(−6)		S^{2+}	6312.10 Å	1.03(0) ± 2.19(−2)	6.19(−6) ± 9.21(−7)
			Average	**3.60(−5) ± 1.27(−6)**			9068.60 Å	1.26(+1) ± 5.96(−1)	4.90(−6) ± 3.88(−7)
			ICF(N(CEL))	3.09 ± 0.17			18.71 μm	1.39(+1) ± 4.65(−1)	5.60(−6) ± 8.07(−7)
				1.11(−4) ± 7.39(−6)			33.48 μm	3.52(0) ± 2.72(−1)	5.63(−6) ± 1.31(−6)
O(CEL)	O^0	5577.34 Å	2.19(−1) ± 4.49(−3)	6.06(−5) ± 3.96(−6)				**Average**	**5.34(−6) ± 6.98(−7)**
		6300.30 Å	1.61(+1) ± 3.39(−1)	6.06(−5) ± 2.48(−6)		S^{3+}	10.51 μm	7.76(0) ± 2.66(−1)	4.18(−7) ± 6.52(−8)
		6363.78 Å	5.10(0) ± 1.11(−1)	6.00(−5) ± 2.46(−6)				ICF(S)	1.00
			Average	**6.05(−5) ± 2.49(−6)**					**6.82(−6) ± 7.13(−7)**
	O^+	3726.03 Å	1.01(+2) ± 2.62(0)	2.67(−4) ± 1.08(−5)	Ar	Ar^+	6.99 μm	7.43(0) ± 2.53(−1)	7.15(−7) ± 2.48(−8)
		3728.81 Å	3.76(+1) ± 9.79(−1)	2.56(−4) ± 9.88(−6)		Ar^{2+}	5191.82 Å	6.41(−2) ± 3.11(−3)	1.94(−6) ± 3.27(−7)
		7320/7330 Å	3.18(+1) ± 5.56(−1)	2.98(−4) ± 2.32(−5)			7135.80 Å	1.08(+1) ± 3.22(−1)	1.47(−6) ± 1.16(−7)
			Average	**2.70(−4) ± 1.29(−5)**			7751.10 Å	2.63(0) ± 9.57(−2)	1.50(−6) ± 1.23(−7)
	O^{2+}	4363.21 Å	2.46(0) ± 2.96(−2)	1.88(−4) ± 9.02(−6)			9.01 μm	1.30(+1) ± 4.71(−1)	1.70(−6) ± 6.56(−8)
		4931.23 Å	5.46(−2) ± 2.92(−3)	1.80(−4) ± 9.67(−6)				**Average**	**1.59(−6) ± 9.25(−8)**
		4958.91 Å	1.46(+2) ± 3.80(−1)	1.87(−4) ± 1.26(−6)		Ar^{3+}	4711.37 Å	3.39(−2) ± 3.05(−3)	2.12(−8) ± 2.29(−9)
			Average	**1.87(−4) ± 1.39(−6)**			4740.16 Å	6.95(−2) ± 1.72(−3)	2.09(−8) ± 8.27(−10)
			ICF(O(CEL))	1.00				**Average**	**2.10(−8) ± 1.31(−9)**
				4.57(−4) ± 1.30(−5)				ICF(Ar)	1.00
Ne	Ne^+	12.81 μm	4.67(+1) ± 1.55(0)	7.23(−5) ± 2.45(−6)					**2.32(−6) ± 9.57(−8)**
	Ne^{2+}	3869.06 Å	4.03(+1) ± 9.46(−1)	8.77(−5) ± 4.07(−6)	Fe	Fe^{2+}	4658.05 Å	1.11(−1) ± 2.50(−3)	6.71(−8) ± 2.80(−9)
		3967.79 Å	1.00(+1) ± 2.16(−1)	7.22(−5) ± 3.29(−6)			4701.53 Å	4.65(−2) ± 3.17(−3)	7.17(−8) ± 5.65(−9)
		15.56 μm	9.67(+1) ± 3.19(0)	8.38(−5) ± 4.54(−6)			4733.91 Å	2.58(−2) ± 2.74(−3)	8.82(−8) ± 1.01(−8)
		36.02 μm	6.18(0) ± 3.23(−1)	8.57(−5) ± 1.01(−5)			4754.69 Å	2.86(−2) ± 3.64(−3)	9.18(−8) ± 1.21(−8)
			Average	**8.41(−5) ± 4.56(−6)**			5270.40 Å	5.89(−2) ± 2.40(−3)	6.76(−8) ± 3.48(−9)
			ICF(Ne)	1.00				**Average**	**7.26(−8) ± 5.11(−9)**
				1.56(−4) ± 4.77(−6)				ICF(Fe)	2.30 ± 0.14
Cl	Cl^+	8578.69 Å	3.04(−1) ± 1.35(−2)	1.64(−8) ± 8.17(−10)					**1.67(−7) ± 1.57(−8)**
		9123.60 Å	1.03(−1) ± 5.46(−3)	2.12(−8) ± 1.23(−9)					
			Average	**1.76(−8) ± 9.22(−10)**					
	Cl^{2+}	5517.72 Å	1.17(−1) ± 3.39(−3)	1.02(−7) ± 3.71(−8)					
		5537.89 Å	2.40(−1) ± 4.59(−3)	1.02(−7) ± 3.93(−8)					
		8434.00 Å	7.76(−3) ± 1.23(−3)	1.18(−7) ± 7.51(−8)					
		8500.20 Å	9.76(−3) ± 3.70(−3)	1.18(−7) ± 8.55(−8)					
			Average	**1.03(−7) ± 4.06(−8)**					
			ICF(Cl)	1.01 ± 0.06					
				1.21(−7) ± 4.16(−8)					

Table 6
The Ionic Abundances Derived Using RLs

Elem. (X)	Ion (X^{m+})	$\lambda_{lab.}$ (Å)	$I(\lambda)$ ($I(H\beta) = 100$)	$n(X^{m+})/n(H^+)$
He	He^+	4120.81	1.77(−1) ± 4.80(−3)	9.95(−2) ± 5.32(−3)
		4387.93	4.39(−1) ± 6.42(−3)	7.18(−2) ± 4.73(−3)
		4437.55	6.64(−2) ± 4.31(−3)	8.53(−2) ± 6.61(−3)
		4471.47	4.63(0) ± 4.85(−2)	9.34(−2) ± 5.22(−3)
		4713.22	6.68(−1) ± 6.70(−3)	1.14(−1) ± 9.20(−3)
		4921.93	1.21(0) ± 4.45(−3)	9.05(−2) ± 4.65(−3)
		5015.68	2.16(0) ± 1.19(−2)	7.69(−2) ± 3.63(−3)
		5047.74	1.68(−1) ± 3.09(−3)	8.24(−2) ± 4.52(−3)
		5875.60	1.47(+1) ± 2.62(−1)	1.02(−1) ± 6.54(−3)
		6678.15	3.97(0) ± 9.94(−2)	9.79(−2) ± 5.74(−3)
		7281.35	7.26(−1) ± 2.30(−2)	8.37(−2) ± 4.43(−3)
			Average	**9.69(−2) ± 5.88(−3)**
			ICF(He)	1.00
				9.69(−2) ± 5.88(−3)
C(RL)	C^{2+}	4267.18	1.03(−1) ± 4.54(−3)	9.66(−5) ± 3.06(−5)
		6578.05	5.05(−2) ± 3.71(−3)	9.84(−5) ± 3.88(−5)
			Average	**9.72(−5) ± 3.33(−5)**
			ICF(C(RL))	1.48 ± 0.22
				1.44(−4) ± 5.38(−5)
N(RL)	N^{2+}	4630.54	2.02(−2) ± 2.59(−3)	9.27(−5) ± 4.21(−5)
		5679.56	1.69(−2) ± 2.30(−3)	4.23(−5) ± 1.93(−5)
			Average	**6.97(−5) ± 3.17(−5)**
			ICF(N(RL))	1.48 ± 0.22
				1.03(−4) ± 4.94(−5)
O(RL)	O^{2+}	4069.62	2.65(−2) ± 3.24(−3)	2.78(−4) ± 7.04(−5)
		4069.88	3.84(−2) ± 4.55(−3)	2.52(−4) ± 6.61(−5)
		4072.15	5.68(−2) ± 2.51(−3)	2.34(−4) ± 5.45(−5)
		4075.86	7.55(−2) ± 5.04(−3)	2.26(−4) ± 5.34(−5)
		4104.99	4.05(−2) ± 4.28(−3)	3.64(−4) ± 9.07(−5)
		4153.30	3.10(−2) ± 1.60(−3)	4.04(−4) ± 9.69(−5)
		4349.43	3.34(−2) ± 2.39(−3)	1.70(−4) ± 3.92(−5)
		4366.90	3.41(−2) ± 2.60(−3)	4.48(−4) ± 1.07(−4)
		4638.86	3.44(−2) ± 3.53(−3)	3.06(−4) ± 7.73(−5)
		4641.81	6.37(−2) ± 2.21(−3)	2.38(−4) ± 5.35(−5)
		4649.13	1.03(−1) ± 2.72(−3)	2.13(−4) ± 4.79(−5)
		4650.84	3.42(−2) ± 1.93(−3)	3.28(−4) ± 7.57(−5)
		4661.63	4.79(−2) ± 2.17(−3)	3.83(−4) ± 8.68(−5)
		4676.23	3.19(−2) ± 5.12(−3)	3.34(−4) ± 9.09(−5)
			Average	**2.82(−4) ± 6.73(−5)**
			ICF(O(RL))	2.45 ± 0.07
				6.89(−4) ± 1.66(−4)

Table 7
Comparison of the Ionic Abundances in 2006 by Us and in 2011 by Arkhipova et al. (2013)

Ion (X^{m+})	$n(X^{m+})/n(H^+)$ in 2006	$n(X^{m+})/n(H^+)$ in 2011
He^+	9.69(−2) ± 5.88(−3)	9.70(−2) ± 8.00(−3)
N^+	3.60(−5) ± 1.27(−6)	5.81(−5) ± 2.31(−5)
O^+	2.70(−4) ± 1.29(−5)	9.10(−5) ± 7.16(−5)
O^{2+}(CEL)	1.87(−4) ± 1.39(−6)	1.01(−4) ± 4.26(−5)
Ne^{2+}	8.41(−5) ± 4.56(−6)	3.46(−5) ± 1.76(−5)
S^+	1.06(−6) ± 1.30(−7)	9.34(−7) ± 5.70(−7)
S^{2+}	5.34(−6) ± 6.98(−7)	1.43(−6) ± 1.13(−6)
Ar^{2+}	1.59(−6) ± 9.25(−8)	1.00(−6) ± 4.26(−7)

metallicity ($0.6\,Z_\odot$). In the Milky Way chemical evolution of such a metallicity, [Fe/H] should be comparable to [α/H]. The expected [Fe/H] is –0.23 from the average [S,Ar/H] ∼ –0.23 if

Table 8
Elemental Abundances

Elem. (X)	$n(X)/n(H)$	$\epsilon(X)$	[X/H]
He	9.69(−2) ± 5.88(−3)	10.99 ± 0.03	+0.06 ± 0.03
C(RL)	1.44(−4) ± 5.38(−5)	8.16 ± 0.16	−0.23 ± 0.17
C(CEL)	9.54(−5) ± 4.26(−5)	7.98 ± 0.19	−0.40 ± 0.20
N(RL)	1.03(−4) ± 7.39(−6)	8.01 ± 0.03	+0.15 ± 0.12
N(CEL)	1.11(−4) ± 7.39(−6)	8.05 ± 0.03	+0.19 ± 0.12
O(RL)	6.89(−4) ± 1.66(−4)	8.84 ± 0.10	+0.11 ± 0.13
O(CEL)	4.57(−4) ± 1.30(−5)	8.66 ± 0.01	−0.07 ± 0.07
Ne	1.56(−4) ± 4.77(−6)	8.19 ± 0.01	+0.14 ± 0.10
S	6.82(−6) ± 7.13(−7)	6.83 ± 0.05	−0.33 ± 0.05
Cl	1.21(−7) ± 4.16(−8)	5.08 ± 0.15	−0.17 ± 0.16
Ar	2.32(−6) ± 9.57(−8)	6.37 ± 0.02	−0.13 ± 0.10
Fe	1.67(−7) ± 1.57(−8)	5.22 ± 0.04	−2.24 ± 0.09

Note. C(CEL) is an expected value estimated by adopting the RL C/O ratio.

all of the Fe atoms are in the gas phase and are not captured by any dust grains. However, the observed [Fe/H] is much smaller than the expected [Fe/H] value. Thus, the largely depleted [Fe/H] suggests that over 99% of the Fe atoms in the nebula would be locked within silicate grains.

3.8. Abundance Discrepancy of C^{2+}, N^{2+}, and O^{2+}

One of the long-standing problems in PN abundances is that the RL C, N, O, and Ne ionic abundances are in general larger than the CEL ones. Several explanations for the abundance discrepancy have been proposed, e.g., temperature fluctuation, high-density clumps, and cold hydrogen-deficient components (see, e.g., a review by Liu 2006). There might be a possible link between the binary central star and the abundance discrepancy, as was recently proposed by Jones et al. (2016). In Hen3-1357, the abundance discrepancy factor (ADF) defined as the ratio of the RL to the CEL ionic abundance is 1.51 ± 0.36 in O^{2+}, which is lower than a typical value ∼2.0 (Liu 2006). Such a degree of the O^{2+} discrepancy can be explained by introducing the temperature fluctuation model proposed by Peimbert (1967).

Parthasarathy et al. (1993) and Feibelman (1995) showed the *IUE* UV spectrum taken on 1992 April 23 (*IUE* Program ID: NA108, PI: S.R. Pottasch, Data-ID: 44459). From there, we can see the CEL C III] 1906/09 Å and N III] 1744-54 Å lines. Although Parthasarathy et al. (1995) gave these line fluxes, the CEL C^{2+} and N^{2+} have never been calculated so far. It would be of interest to estimate the ADF(C^{2+}) because the RL C^{2+} of 6.91(−5) ± 1.48(−6) using the C II 4267 Å line detected in the spectrum taken in 1992 was calculated by Arkhipova et al. (2013). We download the processed SWP44459 data set from the Multimission Archive at STScI (MAST), we measured the fluxes of the C III] 1906/09 Å and N III] 1744-54 Å lines, and calculated the CEL C^{2+} = 9.53 (−5) ± 1.19(−6) and the CEL N^{2+} = 5.49(−5) ± 5.32(−6) using the $F(H\beta)$, $E(B\text{-}V)$, T_e, and n_e reported by Parthasarathy et al. (1993). The ADF(C^{2+}) of 1.24 ± 0.27 in 1992 is similar to our ADF(O) measured in 2006. This might be applied even for ADF(N); the ratio of the RL N^{2+} in 2006 to the CEL N^2 in 1992 is 1.27 ± 0.59.

Based on our analysis, we conclude that the ADF(C/N/O) would be < 2.

3.9. Comparison with AGB Nucleosynthesis Models

The He/C/N/O/Ne/S abundances are close to the AGB star nucleosynthesis model predictions by Karakas (2010) for initially 1.0, 1.25, and 1.5 $M_\odot$ stars with $Z = 0.008$ (0.4 $Z_\odot$). The 1.0 $M_\odot$ model predicts ϵ(He):10.99, ϵ(C):8.09, ϵ(N):7.81, ϵ(O):8.53, ϵ(Ne):7.69, and ϵ(S):7.00. The differences among these models are ϵ(C) and ϵ(N); ϵ(C):8.04 and ϵ(N):7.90 in the 1.25 $M_\odot$ model, and ϵ(C):8.12 and ϵ(N):7.95 in the 1.5 $M_\odot$ model. The predicted final core mass is 0.58 $M_\odot$ in an initially 1.0 $M_\odot$ star to 0.63 $M_\odot$ in a 1.5 $M_\odot$ star.

According to current stellar models for low-mass AGB stars, partial mixing of the bottom of the H-rich convective envelope into the outermost region of the ^{12}C-rich intershell layer leads to the synthesis of extra ^{13}C and ^{14}N at the end of each third dredge-up (TDU). During He-burning, ^{14}N captures two α particles and ^{22}Ne are produced. ^{20}Ne is the most abundant and it is not altered significantly by H or He burning. The ϵ(Ne) discrepancy between the observation (8.19) and the model prediction (7.69) might be due to an increase of ^{22}Ne. The models for the 1.0, 1.25, and 1.5 $M_\odot$ stars with $Z = 0.008$ by Karakas (2010) do not predict TDUs and do not include such partial mixing zone (PMZ). Note that the PMZ is not well justified yet. The Ne abundance in Hen3-1357 suggests that the progenitor might have formed a PMZ and extra ^{22}Ne and Ne might be conveyed to the stellar surface by unexpected mechanisms, e.g., very few TDUs or LTPs. Otherwise, we might interpret that the ϵ(Ne) discrepancy between the observation and the model prediction is due to the errors in the atomic data of $Ne^{+,2+}$.

From chemical abundance analysis, we can conclude that the progenitor mass could be 1.0–1.5 $M_\odot$ if Hen3-1357 had evolved from a star with the initial $Z \sim 0.008$.

4. Photoionization Model with Cloudy

We construct the self-consistent photoionization model using Cloudy to reproduce all of the observed quantities.

The characteristics of the CSPN are critical in the photoionization models because the X-ray to UV wavelength radiation from CSPN determines the ionization structure of the nebula and surrounding ISM and is the ionizing and heating source of gas and dust grains. The distance is necessary for the comparison between the model and the observed fluxes/flux densities/nebula size. In Sections 4.1 and 4.2, therefore, we try to determine parameters of the CSPN and the distance.

The empirically derived quantities of the nebula and the mid-IR SED provide the input parameters of the nebula and dust grain: ϵ(X), geometry, the Hβ flux of the entire nebula, hydrogen density radial profile (n_H) of the nebula, filling factor (f), and type of dust grain. The band flux densities/fluxes, gas emission-line fluxes, and the SED from the UV to far-IR provide constraints in the iterative fitting of the model parameters. In Section 4.3, we explain the input parameters. Finally, we show the modeling result in Section 4.4.

4.1. Flux Density of the CSPN's SED

First, we investigated the SED of the CSPN using the FEROS spectrum, which is the sum of the nebular emission lines and continuum and the CSPN spectrum. For this end, we need to subtract the nebular continuum from the FEROS spectrum. We used the NEBCONT code in the DISPO package of STARLINK v.2015A[12] to generate the nebular continuum. For the calculation, we adopted the Hβ flux of the entire nebula 9.83 (−12) erg s^{-1} cm^{-2}, $n(He^+/H^+)$ = 9.69(−2), T_e = 8090 K, and n_e = 22,860 cm^{-3}, which is the average among n_e([S III]), n_e([Cl III]), n_e([Ne III]), and n_e([Ar IV]).

In the upper panel of Figure 4, we show the synthesized nebular continuum. The discontinuity around 8200 Å indicates the Paschen jump. After we scaled the de-reddened FEROS spectrum up to match with the Hβ line flux of the entire nebula, we manually removed gas emission lines to the extent possible. This gas emission-line-free FEROS spectrum is presented in the same panel. In the lower panel, we show the resultant spectrum generated by subtracting the synthesis nebular continuum spectrum from the gas emission-line-free and flux-density-scaled FEROS spectrum. Note that the residual spectrum coincides with the spectrum of the CSPN. A spike feature around 8200 Å is from the residuals of Paschen and Bracket continuum between the observed and the model. If we can subtract this continuum around the Paschen jump from the

[12] http://starlink.eao.hawaii.edu/starlink

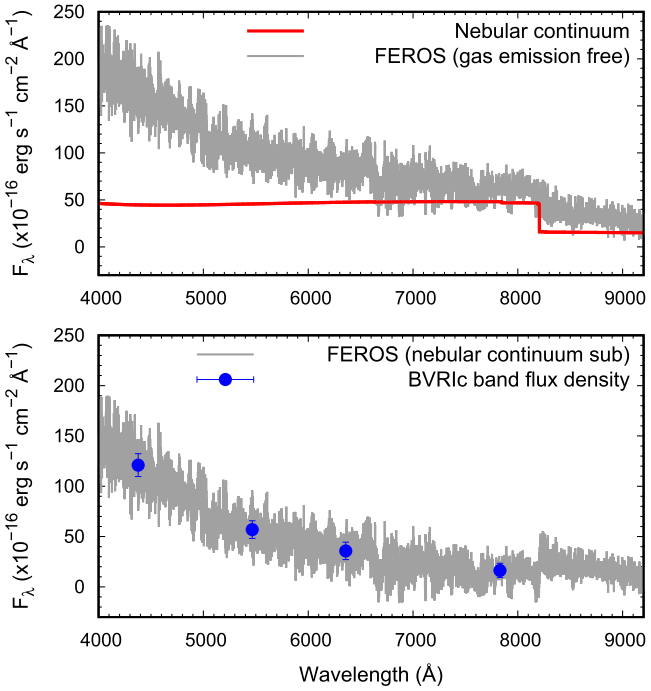

Figure 4. (Upper panel) Gas emission-line-free FEROS spectrum of Hen3-1357 (de-reddened, gray line) and the synthesized nebular continuum by NEBCONT (red line) in the range from 4000 to 9200 Å. (Lower panel) Nebular continuum subtracted FEROS spectrum (gray line) and the de-reddened *BVRIc* band flux densities (blue circles) based on this residual FEROS spectrum.

observed spectrum, the spike feature will be gone. This spike feature does not affect the *Ic*-band magnitude measurement. Using this residual spectrum, we measured flux densities for *BVRIc* bands by taking filter transmission curves of each band, as summarized in Table 9.

4.2. Synthesis of the CSPN's SED, Core Mass, and Distance

Reindl et al. (2014) performed spectral synthesis fitting of the spectrum of the CSPN taken using Far Ultraviolet Spectroscopic Explorer (*FUSE*) in 2006 and obtained $T_{\rm eff} = 55{,}000$ K and $\log\, g = 6.0 \pm 0.5$ cm s^{-2}. However, in our Cloudy model with this $T_{\rm eff}$ and the measured de-reddened m_V of the CSPN (14.51, see Section 4.1) determining the luminosity, we overproduced the fluxes of higher IP ions such as [Ne III] and [O III] lines.[13]

It might be because the nebula ionization structure is not yet fully changed by the recent very fast post-AGB evolution of the CSPN. Although we firmly believe the results of Reindl et al. (2014), we needed to adopt a SED of the CSPN with a lower $T_{\rm eff}$ to reproduce the overall observed nebular line fluxes. For instance, we estimated $T_{\rm eff}$ to be 50,560 ± 2710 K using the [O III]/Hβ line ratio and the formula established among PNe in the Large Magellanic Cloud by Dopita & Meatheringham (1991).

[13] For example, when we adopt $T_{\rm eff} = 55{,}000$ K and distance $D = 2.5$ kpc, the Cloudy model predicted that the respective I([Ne III] 3869 Å) and I([O III] 5007 Å) are 134.6 (40.3 in our FEROS observation) and 303.4 (145.5), and the predicted ionization boundary radius was 4.″1 (1.″28 measured from the *HST*/WFPC2 Hβ image, see Section 4.3.2). Maybe, if we set $D > 8.0$ kpc, the $T_{\rm eff} = 55{,}000$ model could explain the observed line fluxes. However, If we set D to be 8 kpc, we will classify Hen3-1357 as a halo PN and estimate the core mass of the central star to be >0.53–0.60 $M_\odot$.

Table 9
BVRIc Band De-reddened Flux Densities of the CSPN's SED Derived from the Residual FEROS Spectrum

λ_c (Å)	Band	F_λ (erg s^{-1} cm^{-2} Å^{-1})
4378.1	Johnson-*B*	1.21(−14) ± 1.14(−15)
5466.1	Johnson-*V*	5.69(−15) ± 8.76(−16)
6358.0	Cousins-*R*	3.58(−15) ± 8.66(−16)
7829.2	Cousins-*I*	1.63(−15) ± 7.08(−16)

Note. The extinction-free *V*-band magnitude (m_V) is 14.51 ± 0.17, where $F_\lambda(m_V = 0)$ is 3.631(−9) erg s^{-1} cm^{-2} Å^{-1}.

Therefore, we utilized the non-local thermodynamic equilibrium (non-LTE) stellar atmospheres modeling code Tlusty (Hubeny 1988)[14] to obtain the SED of the CSPN for our Cloudy model. Using Tlusty, we constructed line-blanketed, plane-parallel, and hydrostatic stellar atmosphere, where we considered the He, C, N, O, Ne, Si, P, S, and Fe abundances. We run a grid model to cover $T_{\rm eff}$ from 43,000 to 53,000 K in a constant 1000 K steps. Here, we adopted the observed nebular ϵ(He), ϵ(N(CEL)), ϵ(O(CEL)), ϵ(Ne), and ϵ(S). We adopted the expected ϵ(C(CEL)) = 7.98 (see Table 8). As Reindl et al. (2014) reported, there is no significant difference between the nebular and stellar He, C, N, O, S abundances. We adopted stellar ϵ(Si) = 7.52 and ϵ(P) = 4.42 derived by Reindl et al. (2014). From the nebular $\langle$[S, Ar/H]$\rangle = -0.23$, we adopted ϵ(Fe) = 7.23. We interpret that 99% of the Fe atoms in the stellar atmosphere are eventually locked as dust grains in the nebula. We set the microturbulent velocity to 10 km s^{-1} and the rotational velocity to 20 km s^{-1}.

Based on Reindl et al. (2014, 2017), Parthasarathy et al. (1993), and Karakas (2010), the core mass of the CSPN (m_*) is ~0.53–0.6 $M_\odot$. Referring to the theoretical post-AGB evolution tracks presented in Figure 4 of Reindl et al. (2017), we adopted $\log\, g = 5.25$ cm s^{-2} and the distance $D = 2.5$ kpc to obtain $m_* \sim 0.53$–$0.6\, M_\odot$. D has been determined in the range between 826 pc (see Reindl et al. 2017, reference therein) and 5.85 kpc (Frew et al. 2016) thus far. When we adopt $D = 826$ pc, we have to set a very small inner radius of the nebula to reproduce the observed Hβ flux and by doing so, we overproduced fluxes of higher IP lines and obtained hotter dust temperatures, accordingly causing lower dust continuum fluxes. If D is 5.0 kpc, the situation would become better than the case of $D = 826$ pc, and we can then reproduce the observed line fluxes. However, we must set $\log\, g \sim 4.5$ cm s^{-2} in order to obtain a value above the m_* range, and Hen3-1357 would be classified as a halo PN not a thin disk PN.

We verified our adopted D of 2.5 kpc. Following Quireza et al. (2007), we can classify Hen3-1357 into a Type II or III PN based on the observed ϵ(He) and N/O ratio. Hen3-1357 would be a thin disk population. Quireza et al. (2007) reported that the average peculiar velocity relative to the Galaxy rotation (ΔV) is ~23 km s^{-1} for Type IIb and ~70 km s^{-1} for Type III and the average height from the Galactic plane ($|z|$) is ~0.225 kpc for Type IIa and ~0.686 kpc for Type III, respectively. From the constraint on $|z|$, we obtained a range of D toward Hen3-1357 between 1.07 and 3.27 kpc. Maciel & Lago (2005) calculated the rotation velocities at the nebula Galactocentric positions calculated for a Galaxy disk rotation curve based on four distance scales. Using their established

[14] http://nova.astro.umd.edu

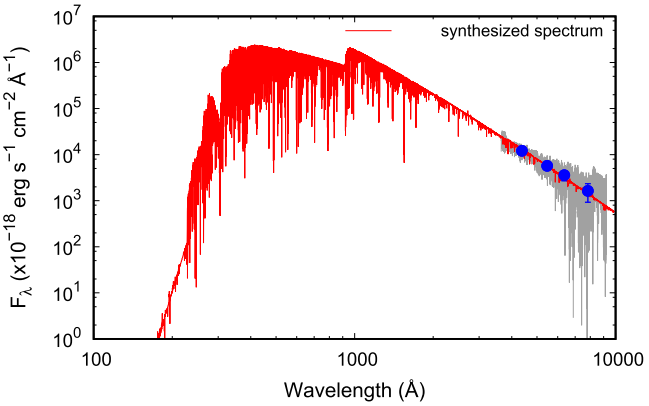

Figure 5. Spectrum of the CSPN synthesized using Tlusty (red line) in $T_{\rm eff} = 45{,}000$ K and $\log g = 5.25$ cm s^{-2}. The flux density is scaled down to the $F_\lambda = 5.69(-15)$ erg s^{-1} cm^{-2} Å^{-1} at 5466.1 Å. The gray line and blue circles are the same as indicated in Figure 4.

Galaxy rotation velocity based on the distance scale of Cahn et al. (1992), van de Steene & Zijlstra (1995), and Zhang (1995), Equation (3) of Quireza et al. (2007), and our measured LSR radial velocity 12.29 km s^{-1} (see Section 3.3), we obtained a D versus ΔV plot. Using this plot and the constraint on ΔV, we got another range of D between 1.63 and 4.92 kpc. Thus, we obtained $D = 1.63$–3.27 kpc, with 2.5 kpc in the middle value of this distance range. From the above discussion, we adopted $D = 2.5$ kpc and the absolute V-band magnitude of the CSPN $M_V = 2.555$.

Finally, we obtained the synthesized spectra using SYNSPEC,[15] as displayed in Figure 5.

4.3. Parameters of the Nebular Gas and Dust Grain

4.3.1. Nebular Elemental Abundances

We adopted elemental abundances listed in Table 8 as a first guess. We refined these abundances to reproduce the observed emission-line intensities. For the other elements unseen in the FEROS and *Spitzer*/IRS spectra, we referred to the predicted values in the AGB nucleosynthesis model for initially 1.5 $M_\odot$ stars with $Z = 0.008$ by Karakas (2010). For the sake of consistency, we substituted the transition probabilities and effective collision strengths of CELs by the same values applied in our nebular abundance analysis.

In spite of non-detection in the *Spitzer*/IRS spectrum, our Cloudy model with ϵ(Si) predicted by the AGB nucleosynthesis model overestimated the [Si III] 34.82 μm line. This indicates that most of the Si atoms exist as amorphous silicate dust grains. Therefore, we took care of the Si and Mg abundances as silicate grain components. Assuming that the nebular [Mg,Si/H] is comparable to the [Mg/H] $= -1.69$ measured in PN IC4846 (Hyung et al. 2001), we kept ϵ(Mg) $= 5.86$ and ϵ(Si) $= 5.84$, respectively. As we discuss later, IC4846 displays amorphous silicate features (e.g., Stanghellini et al. 2012) and very similar elemental abundances to Hen3-1357.

[15] http://nova.astro.umd.edu/Synspec49/synspec.html

Table 10
The Best-fit Cloudy Model Parameters of Hen3-1357

Parameters of the CSPN	Value
$L_*/T_{\rm eff}/\log g/D$	330 $L_\odot$/45,550 K/5.25 cm s^{-2}/2.5 kpc
M_V	2.555
R_*	0.291 $R_\odot$
m_*	0.550 $M_\odot$
Parameters of the Nebula	**Value**
ϵ(X)	He:10.97, C:8.18, N:7.89, O:8.58, Ne:8.20 Mg:5.86, Si:5.84, S:6.74, Cl:4.73, Ar:6.25 Fe:5.23, Others: Karakas (2010)
Geometry	Spherical symmetry
Shell size	$r_{\rm in}$:0.″44 (0.005 pc), $r_{\rm out}$:2.″77 (0.034 pc)
Ionization boundary radius ($r_{\rm ib}$)	1.″48 (0.018 pc)
Filling factor (f)	0.58
$n_{\rm H}$	11 610 cm^{-3}
F(Hβ)	9.84(−12) erg s^{-1} cm^{-2} (de-reddened)
m_g	3.81(−2)$M_\odot$
Parameters of the Dust	**Value**
Grain size	0.01–0.50 μm
T_d	40–150 K
m_d	1.98(−4)$M_\odot$
m_d/m_g (DGR)	5.20(−3)

4.3.2. Nebula Geometry, Boundary Conditions, and Gas Filling Factors

We adopted a spherical shell with a uniform hydrogen density. We assumed the ionization boundary radius ($r_{\rm ib}$) of ∼1.″3 using a plot of count versus size of the circular aperture generated by the archival *HST*/Wide Field Planetary Camera 2 (WFPC2) F487N (Hβ) image taken on 1996 March 3 (Prop-ID: GO6039, PI: M. Bobrowsky). 85% of the total count is measured within the radius of 1.″28. Although the exact size of the nebula in 2006 is unknown, slow nebula shell expansion velocity suggests that the size of the nebula is not largely different since 1996. Here, we measured twice the expansion velocities (2 $V_{\rm exp}$) using Equation (3) of Otsuka et al. (2003, 2009, 2015) and 144 emission lines as summarized in Table 17. To calculate line broadening by gas thermal motion, we adopted a suitable $T_{\rm e}$ for each ion by referring to Table 4. In Hen3-1357, $2V_{\rm exp}$ did not correlate with the IP. We measured the average $2V_{\rm exp} = 14.8 \pm 0.5$ km s^{-1} among the 39 H I lines, which is consistent with the mean expansion velocity ($V_{\rm exp}$) of 8.4 ± 1.5 km s^{-1} measured from the 17 lines by Arkhipova et al. (2013).

The filling factor f can be defined as the ratio of an rms density derived from a hydrogen line flux, $T_{\rm e}$, and nebula radius to the $n_{\rm e}$(CELs) (see, e.g., Mallik & Peimbert 1988; Peimbert et al. 2000). We calculated an rms density of 10 750 cm^{-3} from the Hβ flux of the entire nebula, $T_{\rm e} = 8060$ K, $r_{\rm ib} = 1.''28$, and a constant $n_{\rm e}/n({\rm H}^+) = 1.15$. We estimated f to be 0.47–0.62 using this rms density and the observed $n_{\rm e}$(CELs). Here, we set $f = 0.55$ as a first guess and varied.

4.3.3. Dust Grains and Size Distribution

We assumed spherical-shaped silicate grains and adopted a standard interstellar size distribution ($n(a) \propto a^{-3.5}$, Mathis et al. 1977) with radius $a = 0.01$–0.50 μm. We selected the

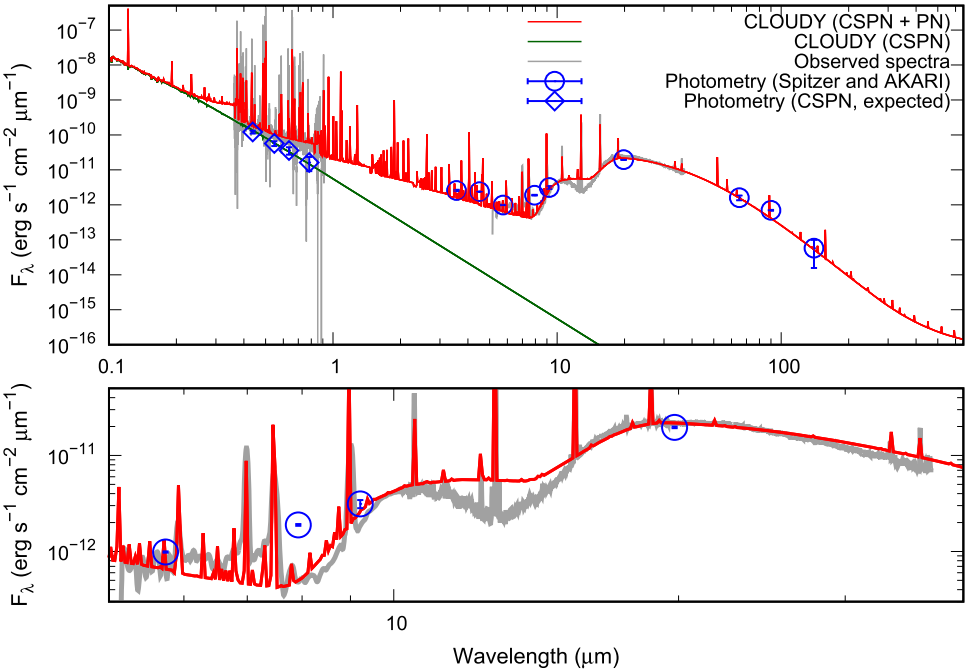

Figure 6. (Upper panel) Comparison between the Cloudy model and observational data of Hen3-1357. The blue diamonds indicate the observed *BVRIc* band flux densities of the CSPN, which are the same values in listed in Table 9. (Lower panel) Closed-up plots in 5-40 μm. In both panels, we set the spectral resolution of the synthesized Cloudy spectrum to be a constant 600, corresponding to that of *Spitzer*/IRS SH and LH spectra.

Table 11
Comparison of the ICFs between the Observation and the Cloudy Model

Elem.	ICF(obs)	ICF(model)
He	1.00	1.03
C(RL)	1.48 ± 0.22	1.30
N(RL)	1.48 ± 0.22	1.62
N(CEL)	3.09 ± 0.17	2.69
O(RL)	2.45 ± 0.07	2.23
O(CEL)	1.00	1.04
Ne	1.00	1.01
S	1.00	1.00
Cl	1.00 ± 0.06	1.01
Ar	1.00	1.01
Fe	2.30 ± 0.14	2.07

dielectric function table of astronomical silicate currently recommended by the webpage of B. Draine.[16]

4.4. Model Result

To find the best-fit model, we varied $T_{\rm eff}$, the inner radius of the nebula $r_{\rm in}$, $n_{\rm H}$, ϵ(He/C/N/O/Ne/S/Cl/Ar/Fe), the dust mass fraction, and f within a given range using the optimize command available in Cloudy.

García-Hernández et al. (2002) found that the distribution of molecular hydrogen H_2 $v = 1$-0 S(1) at 2.122 μm and $v = 2$-1S (1) at 2.248 μm is quite homogeneous and extends well beyond the distribution of the H I Brγ line. This suggests that Hen3-1357 has large neutral regions.

Thus, we went to deep neutral gas regions in our model; we continued calculation until any of the model's predicted flux densities at *AKARI*/FIS 65/90/140 μm bands reached or exceeded the relevant observed values. The Cloudy model predicted $r_{\rm ib} = 1\farcs48$ where $T_{\rm e}$ drops below 4000 K. We stopped our model calculation at the outer radius ($r_{\rm out}$) of 3.4 (−2) pc ($2\farcs77$). The goodness of fit was determined by the reduced χ^2 value calculated from the following observational constraints: 17 broadband fluxes, 5 broadband flux densities, 104 gas emission fluxes, $r_{\rm ib}$, de-redden $F(\rm H\beta)$ of the entire nebula. Table 10 summarizes the parameters of the best-fit model, where the reduced χ^2 is 33.5.

The SED of the best-fit model, in comparison with the observational data, is presented in Figure 6. From the model result we confirmed that the gas-emission contribution to *Spitzer*/IRAC 8.0 μm and *AKARI*/IRC 9.0/18 μm bands is 51.8%, 19.1%, and 3.9%, respectively. Thus, the disagreement at the *Spitzer*/IRAC 8.0 μm band between the observed photometry and the predicted SED can be explained by considering the gas-emission contribution to the relevant band.

The observed and model-predicted line fluxes, band fluxes, and band flux densities are summarized in Table 18. The intensity of the O II 4075 Å and 4651 Å is the sum of the multiplet V10 and V1 O II lines, respectively. It is noteworthy that we simultaneously reproduced both the observed RL/CEL N and O line fluxes.

The predicted ICF(X) by Cloudy listed in Table 11 is in excellent agreement with the ICF(X) derived in Section 3.7, indicating that our Cloudy model succeeded in explaining the ionization nebula structure and the ICF(X) based on IP is the proper value.

As described in Section 4.2, under the constraints of the CSPN at $D = 2.5$ kpc, we need $T_{\rm eff} = 45{,}550$ K and $L_* = 330\,L_\odot$ in order to explain the observed quantities. With D, L_*, and log g, we derived $m_* = 0.55\,M_\odot$.

The gas mass (m_g) = 3.81(−2) $M_\odot$ is the sum of the ionized and neutral gas masses. The ionized gas mass is 5.38(−3) $M_\odot$ and the remaining is the neutral gas mass. Our derived m_g is close to the ejected mass, which equals 8.9(−2) $M_\odot$ in initially 1.5 $M_\odot$ stars with $Z = 0.008$ during the last thermal pulse

[16] https://www.astro.princeton.edu/~draine/dust/dust.diel.html

Table 12
Comparisons with the ϵ(X) of IC4846 and the Average ϵ(X) Value Among Galactic Amorphous Silicate-rich PNe

Elem. (X)	OD PN Ave.	IC4846 (a)	(b)	(c)	(d)	(e)	Ave.	Hen 3-1357
He	11.02	10.98	10.96	10.90	11.01	⋯	10.96	10.99
C(RL)	⋯	7.74	8.37	8.43	⋯	⋯	8.27	8.16
C(CEL)	⋯	7.68	8.45	8.16	⋯	7.95	8.15	7.98
N(RL)	⋯	⋯	⋯	8.10	⋯	⋯	8.10	8.01
N(CEL)	7.78	7.89	7.81	8.09	7.69	⋯	7.90	8.05
O(RL)	⋯	⋯	8.97	8.78		⋯	8.89	8.84
O(CEL)	8.42	8.60	8.51	8.59	8.60	8.50	8.56	8.66
Ne	7.78	7.90	7.83	7.77	7.99	⋯	7.88	8.19
Mg	⋯	5.86	⋯	⋯	⋯	⋯	5.86	⋯
S	6.50	6.95	6.63	7.01	6.73	⋯	6.86	6.83
Cl	6.15	5.11	⋯	5.34	6.14	⋯	5.76	5.08
Ar	6.03	6.18	5.96	6.02	6.13	⋯	6.08	6.37
Fe	⋯	⋯	⋯	⋯	⋯	5.21	5.21	5.22

Note. The ϵ(X) of Hen3-1357 is the result using the ICFs, except for the CEL C, which is an expected value. The average abundance of Galactic amorphous silicate-rich PNe in the Galaxy (OD PN Ave) in the second column is taken from García-Hernández & Górny (2014). On elemental abundances of the PN IC4846 in the third—seventh columns—(a) Hyung et al. (2001), (b) Wesson et al. (2005), (c) Wang & Liu (2007), (d) García-Hernández & Górny (2014), and (e) Delgado-Inglada & Rodríguez (2014). The eighth column is the average among the measurements by (a)–(e).

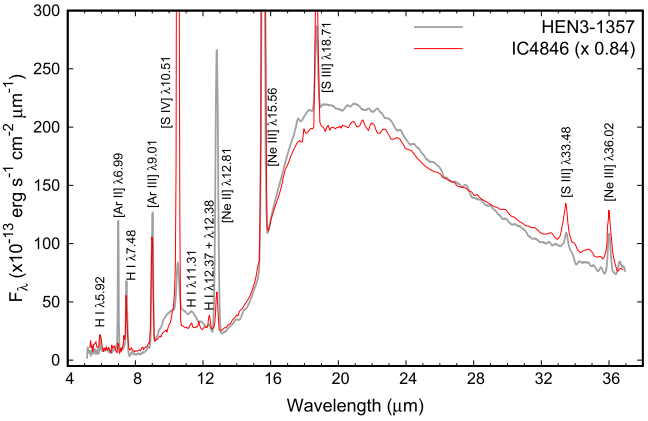

Figure 7. *Spitzer*/IRS spectra of IC4846 and Hen3-1357. The spectral resolution of Hen3-1357 is down to match with that of IC4846. For IC4846, we scaled the flux density up to match with *AKARI*/IRC 9.0/18 μm bands (0.1311 and 2.038 Jy, respectively; Yamamura et al. 2010). For demonstration, the flux density of this scaled spectrum is further scaled to match with the IRS spectrum of Hen3-1357 by a constant factor of 0.84. See the text for details.

AGB, predicted by Karakas & Lattanzio (2007). We obtained a dust mass (m_d) of 1.98(−4) $M_\odot$.

It is of interest to know how far-IR data impact gas and dust mass estimates in our model. When we stopped model calculations at $r_{\rm ib}$, we obtained $m_g = 4.61(-3)$ $M_\odot$ and $m_d = 3.79(-5)$ $M_\odot$. This model did not well fit any *AKARI* far-IR fluxes. To fit the observed far-IR data, we need a larger $r_{\rm out}$. With the *AKARI* far-IR data, we obviously obtained much greater m_g and m_d. About 80% of the total dust mass is from warm–cold dust components beyond the ionization front. From the model results, we confirmed that the gas-emission contribution to *AKARI*65/90/140 μm bands is 1.4%, 1.08%, and 2.58%, respectively. *AKARI* far-IR data would be thermal emission from warm–cold dust.

Cox et al. (2011) derived an upper limit of the sum of m_d and $m_g = 0.16\,M_\odot$ within a 3 pc radius using the *AKARI*/90 μm and a constant dust-to-gas mass ratio (DGR) = 6.25(−3) for O-rich dust, although the measured dust temperature (T_d) is unknown. Using their results, we calculated an upper limit $m_g = 0.159\,M_\odot$ and $m_d = 9.94(-4)$ $M_\odot$, respectively.

Umana et al. (2008) derived the total ionized mass of ∼5.7(−2) $M_\odot$ using the radio data in 2002, assuming $D = 5.6$ kpc, inner/outer radii = 0.″65/1.″3 shallow shell geometry, and $f = 1.0$. Using the *IRAS* data, they derived $T_d = 137 \pm 2$ K and $m_d = 2$ (−4) $M_\odot$using the 60 μm flux density in the case of the silicate. Based on the results and assumptions of Umana et al. (2008), ionized gas and co-existing dust would be ∼6.6(−3) $M_\odot$ and ∼4.0 (−5) $M_\odot$, respectively, if we adopt $D = 2.5$ kpc and $f = 0.58$. These estimated values are consistent with our derived m_g and m_d when we stopped the model at $r_{\rm ib}$. On the dust, Cox et al. (2011) found that the *AKARI* far-IR flux densities are a factor two lower than predicted from the *IRAS* data. They interpreted that the far-IR variability in its infrared flux might occur due to recent mass-loss event(s) or evolution of the CSPN. Following the report of Cox et al. (2011) and the dust mass ∼4.0(−5) $M_\odot$ co-existing with the ionized gas by the *IRAS* data in 1980s, we estimate the dust mass to be $\lesssim$2(−5) $M_\odot$ in 2006–2007, which is comparable to our derived dust mass of 3.79(−5) $M_\odot$ within the ionized gas.

5. Discussion

It is necessary to verify whether the gas and dust chemistry in Hen3-1357 is consistent with other O-rich gas and dust Galactic PNe. To compare such PNe is an important step in understanding the evolution of Hen3-1357.

García-Hernández & Górny (2014) investigated relations among dust features, elemental abundances, and evolution of the progenitors. In the second column of Table 12, we list the average ϵ(X) among their amorphous silicate PNe. They found that ϵ(He) and the N/O ratio in these amorphous silicate-containing PNe are in agreement with the AGB nucleosynthesis model predictions for initially ∼1.0 $M_\odot$ stars with $Z = 0.008$. García-Hernández & Górny (2014) suggested that the higher Ne/O ratios in O-rich dust PNe relative to the AGB models may reflect the effect of the PMZ. The observed ϵ(He) and the CEL N/O ratio of 0.24 ± 0.02 in Hen3-1357 coincide with the average values in their amorphous silicate PN sample. As discussed in Section 3.9, our predicted progenitor mass, initial metallicity, and interpretation for the Ne overabundance in Hen3-1357 follow their results.

We can now understand relations among dust features, nebular abundances, and the progenitor stars' evolution. Moreover, we know that the nebula morphology is connected to the central star's evolution. Using the *HST*/WFPC images as a guide, we tried to find objects showing similar nebula shape, dust features, and elemental abundance patterns to Hen3-1357. To our best knowledge, the point-symmetric PN IC4846 (e.g., Miranda et al. 2001) is very similar to Hen3-1357.

IC4846 clearly shows amorphous silicate features, as reported by Stanghellini et al. (2012). We reduced the BCD of IC4846 (obs AORKEY: 25839616, PI: L. Stanghellini) with the same process applied for Hen3-1357. In Figure 7, we display the *Spitzer*/IRS spectra of IC4846 and Hen3-1357. The dust features seen in both PNe are very similar, except for the different strengths of the 9 and 18 μm emission bumps, which might reflect the difference in the grain composition. For IC4846, Stasińska & Szczerba (1999) derived a single $T_d = 107$ K and DGR $= 1.2(-3)$ based on the *IRAS* four band fluxes using a modified blackbody function. Tajitsu & Tamura (1998) derived a single $T_d = 168$ K using the *IRAS* data. Zhang & Kwok (1991) derived a single $T_d = 152$ K and $T_{\rm eff} =$ 47,600 K by fitting SED from *IUE* to *IRAS* data.

In the third to seventh columns of Table 12, we compile nebular abundances of IC4846 measured by prior works. The eighth column gives the average value. Obviously, the abundances in both IC4846 and Hen3-1357 are in excellent agreement even in the RL ϵ(C,N,O) and the Fe-depletion. So far, the ϵ(Mg) and ϵ(Fe) measurements have been performed only by Hyung et al. (2001) using the *IUE* UV spectrum and only by Delgado-Inglada & Rodríguez (2014) using the optical spectra, respectively. The largely depleted [Mg/H] $= -1.69$ in IC4846 might indicate that most of the Mg atoms are captured by silicate grains. We assumed the similar situation to Hen3-1357 in our Cloudy model.

Hyung et al. (2001) succeeded in reproducing UV–optical gas emission-line fluxes in the photoionization model of IC4846 by setting CSPN's radius to $0.425\,R_\odot$, $T_{\rm eff} =$ 70,000 K, $\log g = 4.6$ cm s^{-2}, and $D = 7$ kpc, which gave $L_* = 3900\,L_\odot$. In comparison to post-AGB evolutionary tracks, they estimated $m_* \sim 0.57\,M_\odot$.

From the above comparisons, we can conclude that Hen3-1357 is an ordinary amorphous silicate-rich and O-rich gas PN. Among amorphous silicate-rich PNe in the Milky Way, IC4846 is very similar to Hen3-1357. Both PNe have evolved from similar progenitor mass stars with $Z = 0.008$. However, the rapid evolution of the central star of Hen3-357 still remains a puzzle.

6. Summary

We performed a detailed chemical abundance analysis and constructed the photoionization model of Hen3-1357 to characterize the PN and obtain a coherent picture of the dusty nebula and CSPN in 2006 based on optical to far-IR data.

We calculated the abundances of the nine elements. The RL C/O ratio indicates that Hen3-1357 is an O-rich PN, supported by the detection of the broad 9/18 μm amorphous silicate bands in the *Spitzer*/IRS spectrum. The ADF(O^{2+}) is less than a typical value measured in PNe. The observed elemental abundances can be explained by AGB nucleosynthesis models of Karakas (2010) for initially 1–1.5 $M_\odot$ stars with $Z = 0.008$. The Ne overabundance might be due to the enhancement of ^{22}Ne isotope in the He-rich intershell.

We did not find significant variation of nebular line intensities between 2006 and 2011, suggesting that the nebular ionization state and elemental abundances are most likely in a steady state during the same period, while the central star is rapidly evolving.

By incorporating the spectrum of the CSPN synthesized by Tlusty as the ionization/heating source of the PN with Cloudy modeling, we succeeded in explaining the observed SED and derived the gas and dust masses, dust-to-gas mass ratio, and core mass of the CSPN. About 80% of the total dust mass is from the warm–cold dust components beyond ionization front.

Through comparison with other Galactic PNe, we found that Hen3-1357 is an ordinary amorphous silicate-rich and O-rich gas PN. IC4846 shows many similarities in PN properties with Hen3-1357.

Although we derived physical properties of the nebula and also provided the range of the progenitor mass, the rapid evolution from post-AGB B1 supergiant in 1971 to a young PN in a matter of 21 years is not yet understood. If the central star has experienced LTP, then it should be H-poor ad He- and C-rich in its present hot post-AGB stage soon after the LTP. However, the nebular and stellar chemical compositions calculated by us and Reindl et al. (2014, 2017) are nearly solar, not at all similar to those of LTP PNe. If the central star has now started returning toward the AGB phase, then very soon it will go through A, F, and G spectral types before it appears as a born-again AGB star. If so, it may show abundances similar to that of LTP PNe in the future. We need to monitor the central star's $T_{\rm eff}$, $\log g$, and chemical composition in order to confirm whether it is evolving back toward the AGB stage. If Hen3-1357 is a binary, rapid evolution might be explained. For that end, monitoring of the radial velocity using stellar absorption profiles in UV wavelength would be necessary. Moreover, comparisons with other Galactic amorphous silicate-rich and O-rich gas PNe such as IC4846 can help us to understand the evolution of Hen3-1357. Thus, further observations of both the nebula and the central star are required for further understanding this PN.

We are grateful to the anonymous referee for a careful reading and valuable suggestions. M.O. thanks Prof. Ivan Hubeny for useful suggestions on Tlusty modeling. M.O. was supported by the research fund 104-2811-M-001-138 and 104-2112-M-001-041-MY3 from the Ministry of Science and Technology (*MOST*), R.O.C. This work was partly based on archival data obtained with the *Spitzer* Space Telescope, which is operated by the Jet Propulsion Laboratory, California Institute of Technology under a contract with NASA. This research is in part based on observations with *AKARI*, a JAXA project with the participation of ESA. Support for this work was provided by an award issued by JPL/Caltech. Some of the data used in this paper were obtained from the Mikulski Archive for Space Telescopes (MAST). STScI is operated by the Association of Universities for Research in Astronomy, Inc., under NASA contract NAS5-26555. Support for MAST for non-*HST* data is provided by the NASA Office of Space Science via grant NNX09AF08G and by other grants and contracts. A portion of this work was based on the use of the ASIAA clustering computing system.

Software: IRAF (v.2.16), SMART (v.8.2.9: Higdon et al. 2004), IRSCLEAN (v.2.1.1), MOPEX, STARLINK (v.2015A), CLOUDY (v13.03: Ferland et al. 2013), TLUSTY (Hubeny 1988)

Appendix

The following Tables 13–18 support our analysis.

Table 13
The Identified Atomic Emission Lines in the FEROS Spectrum

$\lambda_{obs.}$ (Å)	Line	$\lambda_{lab.}$ (Å)	$f(\lambda)$	$I(\lambda)$ ($I(H\beta) = 100$)	$\delta I(\lambda)$
3697.33	H I (B17)	3697.15	0.328	1.923	0.107
3704.01	H I (B16)	3703.85	0.327	2.028	0.122
3705.16	He I	3704.98	0.327	0.965	0.087
3712.12	H I (B15)	3711.97	0.325	2.384	0.119
3722.02	H I (B14)	3721.94	0.323	4.156	0.155
3723.81	Fe II]	3723.92	0.323	0.474	0.058
3726.20	[O II]	3726.03	0.322	101.210	2.625
3728.96	[O II]	3728.81	0.322	37.647	0.979
3734.52	H I (B13)	3734.37	0.321	3.026	0.097
3750.31	H I (B12)	3750.15	0.317	4.220	0.124
3770.79	H I (B11)	3770.63	0.313	4.353	0.115
3798.05	H I (B10)	3797.90	0.307	5.330	0.133
3819.79	He I	3819.60	0.302	1.142	0.033
3833.75	He I	3833.55	0.299	0.072	0.010
3835.54	H I (B9)	3835.38	0.299	7.597	0.183
3867.69	He I	3867.47	0.291	0.147	0.008
3868.92	[Ne III]	3869.06	0.291	40.325	0.946
3871.95	He I	3871.79	0.290	0.078	0.006
3889.06	H I (B8)	3889.05	0.286	15.997	0.472
3926.71	He I	3926.54	0.277	0.124	0.005
3964.90	He I	3964.73	0.267	0.540	0.012
3967.63	[Ne III]	3967.79	0.267	10.000	0.216
3970.23	H I (B7)	3970.07	0.266	16.026	0.341
4009.42	He I	4009.26	0.256	0.152	0.006
4026.37	He I	4026.20	0.251	1.532	0.031
4068.77	[S II]	4068.60	0.239	4.471	0.086
4069.74	O II	4069.62	0.239	0.027	0.003
4070.04	O II	4069.88	0.239	0.038	0.005
4072.32	O II	4072.15	0.238	0.057	0.003
4076.02	O II	4075.86	0.237	0.076	0.005
4076.52	[S II]	4076.35	0.237	1.508	0.029
4097.45	N III	4097.35	0.231	0.023	0.003
4101.90	H I (B6, Hδ)	4101.73	0.230	21.516	0.395
4103.19	O II	4103.00	0.229	0.030	0.004
4103.81	N III	4103.39	0.229	0.028	0.004
4105.13	O II	4104.99	0.229	0.040	0.004
4119.45	O II	4119.22	0.224	0.019	0.004
4121.00	He I	4120.81	0.224	0.177	0.005
4143.93	He I	4143.76	0.217	0.229	0.005
4153.44	O II	4153.30	0.214	0.031	0.002
4267.35	C II	4267.18	0.180	0.103	0.005
4276.00	O II	4275.99	0.177	0.032	0.005
4340.64	H I (B5, Hγ)	4340.46	0.157	46.052	0.579
4349.64	O II	4349.43	0.154	0.033	0.002
4363.38	[O III]	4363.21	0.149	2.461	0.030
4367.08	O II	4366.90	0.148	0.034	0.003
4368.41	O I	4368.24	0.148	0.036	0.002
4388.11	He I	4387.93	0.142	0.439	0.006
4437.76	He I	4437.55	0.126	0.066	0.004
4471.68	He I	4471.47	0.115	4.628	0.048
4591.14	N II	4590.85	0.078	0.036	0.005
4630.71	N II	4630.54	0.066	0.020	0.003
4639.02	O II	4638.86	0.064	0.034	0.004
4642.01	O II	4641.81	0.063	0.064	0.002
4649.33	O II	4649.13	0.061	0.103	0.003
4651.01	O II	4650.84	0.060	0.034	0.002
4658.33	[Fe III]	4658.05	0.058	0.111	0.002
4661.83	O II	4661.63	0.057	0.048	0.002
4676.48	O II	4676.23	0.053	0.032	0.005
4701.86	[Fe III]	4701.53	0.045	0.046	0.003
4711.59	[Ar IV]	4711.37	0.042	0.034	0.003
4713.38	He I	4713.22	0.042	0.668	0.007
4725.73	[Ne IV]?	4725.64	0.038	0.011	0.002
4734.06	[Fe III]	4733.91	0.036	0.026	0.003
4740.41	[Ar IV]	4740.16	0.034	0.070	0.002
4754.94	[Fe III]	4754.69	0.030	0.029	0.004
4861.52	H I (B4, Hβ)	4861.33	0.000	100.000	0.112
4881.20	[Fe III]	4881.00	−0.005	0.045	0.004
4891.21	O II?	4890.86	−0.008	0.032	0.008
4922.13	He I	4921.93	−0.016	1.214	0.004
4924.78	[Fe III]	4924.54	−0.017	0.027	0.002

Table 13
(Continued)

$\lambda_{obs.}$ (Å)	Line	$\lambda_{lab.}$ (Å)	$f(\lambda)$	$I(\lambda)$ ($I(H\beta) = 100$)	$\delta I(\lambda)$
4931.45	[O III]	4931.23	−0.019	0.055	0.003
4959.13	[O III]	4958.91	−0.026	145.519	0.380
4987.58	[Fe III]	4987.21	−0.033	0.016	0.003
4996.95	O II	4996.98	−0.035	0.045	0.004
5015.88	He I	5015.68	−0.040	2.161	0.012
5047.95	He I	5047.74	−0.048	0.168	0.003
5146.79	[Fe III]	5146.45	−0.071	0.027	0.004
5159.01	[Fe II]	5158.78	−0.074	0.017	0.002
5191.94	[Ar III]	5191.82	−0.081	0.064	0.003
5198.13	[N I]	5197.90	−0.082	0.363	0.004
5200.49	[N I]	5200.26	−0.083	0.228	0.004
5270.74	[Fe III]	5270.40	−0.098	0.059	0.002
5517.91	[Cl III]	5517.72	−0.145	0.117	0.003
5538.06	[Cl III]	5537.89	−0.149	0.240	0.005
5577.64	[O I]	5577.34	−0.156	0.219	0.004
5679.81	N II	5679.56	−0.173	0.017	0.002
5754.83	[N II]	5754.64	−0.185	2.578	0.038
5791.58	C II	5791.69	−0.190	0.021	0.002
5875.88	He I	5875.60	−0.203	14.666	0.262
5958.74	O I	5958.54	−0.215	0.026	0.004
6300.55	[O I]	6300.30	−0.263	16.129	0.339
6312.32	[S III]	6312.10	−0.264	1.031	0.022
6364.04	[O I]	6363.78	−0.271	5.095	0.111
6527.42	[N II]	6527.24	−0.293	0.019	0.003
6548.32	[N II]	6548.04	−0.296	40.956	0.967
6578.31	C II	6578.05	−0.300	0.050	0.004
6583.70	[N II]	6583.46	−0.300	121.454	2.915
6678.42	He I	6678.15	−0.313	3.972	0.099
6716.73	[S II]	6716.44	−0.318	6.066	0.154
6721.76	O II	6721.39	−0.319	0.009	0.002
6731.10	[S II]	6730.81	−0.320	12.471	0.319
7002.42	O I	7002.12	−0.356	0.051	0.004
7062.57	He I	7062.28	−0.364	0.019	0.003
7065.50	He I	7065.18	−0.364	7.846	0.247
7136.06	[Ar III]	7135.80	−0.374	10.767	0.322
7155.53	[Fe II]	7155.16	−0.376	0.034	0.003
7160.85	He I	7160.61	−0.377	0.027	0.003
7254.70	O I	7254.45	−0.390	0.064	0.004
7281.64	He I	7281.35	−0.393	0.726	0.023
7298.33	He I	7298.04	−0.395	0.035	0.003
7319.33	[O II]	7318.92	−0.398	3.998	0.130
7320.40	[O II]	7319.99	−0.398	13.487	0.430
7329.96	[O II]	7329.66	−0.400	7.476	0.239
7331.04	[O II]	7330.73	−0.400	6.987	0.224
7378.30	[Ni II]	7377.83	−0.406	0.030	0.003
7500.18	He I	7499.85	−0.422	0.036	0.004
7751.42	[Ar III]	7751.10	−0.455	2.630	0.096
7816.45	He I	7816.14	−0.464	0.077	0.003
8245.95	H I (P42)	8245.64	−0.516	0.033	0.004
8248.09	H I (P41)	8247.73	−0.516	0.027	0.003
8250.17	H I (P40)	8249.97	−0.517	0.028	0.001
8252.65	H I (P39)	8252.40	−0.517	0.033	0.002
8255.36	H I (P38)	8255.02	−0.517	0.027	0.002
8258.21	H I (P37)	8257.85	−0.517	0.041	0.002
8261.20	H I (P36)	8260.93	−0.518	0.042	0.002
8264.69	He I	8264.62	−0.518	0.059	0.003
8268.31	H I (P34)	8267.94	−0.519	0.055	0.003
8272.22	H I (P33)	8271.93	−0.519	0.057	0.003
8276.60	H I (P32)	8276.31	−0.520	0.070	0.004
8281.49	H I (P31)	8281.12	−0.520	0.072	0.004
8286.71	H I (P30)	8286.43	−0.521	0.111	0.005
8292.67	H I (P29)	8292.31	−0.521	0.096	0.005
8299.20	H I (P28)	8298.83	−0.522	0.118	0.005
8306.48	H I (P27)	8306.11	−0.523	0.119	0.005
8314.61	H I (P26)	8314.26	−0.524	0.128	0.006
8323.76	H I (P25)	8323.42	−0.525	0.143	0.006
8334.11	H I (P24)	8333.78	−0.526	0.152	0.007
8342.74	C III	8342.20	−0.527	0.020	0.002
8345.85	H I (P23)	8345.55	−0.527	0.188	0.008
8359.31	H I (P22)	8359.00	−0.529	0.220	0.009
8362.07	He I	8361.73	−0.529	0.082	0.004

Table 13
(Continued)

$\lambda_{obs.}$ (Å)	Line	$\lambda_{lab.}$ (Å)	$f(\lambda)$	$I(\lambda)$ ($I(\mathrm{H}\beta) = 100$)	$\delta I(\lambda)$
8374.81	H I (P21)	8374.48	−0.531	0.219	0.009
8392.73	H I (P20)	8392.40	−0.533	0.252	0.011
8397.80	He I	8397.42	−0.533	0.010	0.001
8413.65	H I (P19)	8413.32	−0.535	0.288	0.012
8434.02	[Cl III]	8434.00	−0.537	0.008	0.001
8438.29	H I (P18)	8437.95	−0.537	0.326	0.014
8444.79	He I	8444.55	−0.538	0.025	0.003
8446.82	O I	8446.48	−0.538	0.468	0.020
8451.52	He I	8451.17	−0.539	0.013	0.003
8467.58	H I (P17)	8467.25	−0.541	0.378	0.016
8486.63	He I	8480.79	−0.543	0.017	0.002
8500.45	[Cl III]	8500.20	−0.544	0.010	0.004
8502.82	H I (P16)	8502.48	−0.544	0.450	0.020
8545.71	H I (P15)	8545.38	−0.549	0.508	0.023
8579.06	[Cl II]	8578.69	−0.552	0.304	0.014
8582.21	He I	8581.88	−0.552	0.024	0.003
8598.73	H I (P14)	8598.39	−0.554	0.636	0.028
8617.23	[Fe II]	8616.95	−0.556	0.042	0.002
8648.62	He I	8648.26	−0.559	0.030	0.002
8665.37	H I (P13)	8665.02	−0.560	0.829	0.037
8680.62	N I	8680.28	−0.562	0.017	0.001
8683.85	N I	8683.40	−0.562	0.017	0.001
8703.64	N I	8703.25	−0.564	0.012	0.001
8727.55	[C I]	8727.12	−0.566	0.014	0.002
8733.82	He I	8733.44	−0.567	0.037	0.003
8736.36	He I	8736.04	−0.567	0.012	0.002
8750.82	H I (P12)	8750.47	−0.568	1.042	0.047
8777.05	He I	8776.83	−0.571	0.053	0.003
8845.72	He I	8845.39	−0.576	0.055	0.004
8892.21	[Fe II]	8891.91	−0.580	0.016	0.002
8997.34	He I	8997.00	−0.588	0.055	0.004
9000.05	He I	8999.75	−0.589	0.022	0.002
9015.29	H I (P10)	9014.91	−0.590	1.624	0.077
9052.33	[Fe II]	9051.95	−0.592	0.011	0.002
9063.71	He I	9063.32	−0.593	0.060	0.004
9069.29	[S III]	9068.60	−0.594	12.577	0.596
9123.99	[Cl II]	9123.60	−0.598	0.103	0.005
9210.69	He I	9210.34	−0.604	0.099	0.006

Note. The first column is the wavelength at the observation. The third column is the wavelength at rest in the laboratory.

Table 14
The Identified Lines in the *Spitzer*/IRS Spectrum

$\lambda_{lab.}$ (μm)	Line	$I(\lambda)$ ($I(\mathrm{H}\beta) = 100$)
5.92	H I	0.740 ± 0.042
6.99	[Ar II]	7.435 ± 0.253
7.48	H I	6.186 ± 0.223
9.01	[Ar III]	12.993 ± 0.471
10.51	[S IV]	7.758 ± 0.266
11.31	H I	0.277 ± 0.068
12.37	H I	1.043 ± 0.034
12.81	[Ne II]	46.711 ± 1.553
14.37	[Cl II]?	0.323 ± 0.040
15.56	[Ne III]	96.699 ± 3.188
17.62	He I?	1.274 ± 0.094
18.71	[S III]	13.864 ± 0.465
33.48	[S III]	3.517 ± 0.272
36.02	[Ne III]	6.180 ± 0.323

Note. The flux density is scaled-up to match with the *AKARI*/IRC 9.0 μm band flux density. Then, the fluxes of these identified atomic lines are normalized with respect to the Hβ flux of the entire nebula 9.83(−12) ± 7.33 (−13) erg s^{-1} cm^{-2}. See the text for details.

Table 15
Comparison of the Overlapped Line Fluxes between our 2006 and Arkhipova et al. (2013)'s 2011 Observations

$\lambda_{lab.}$ (Å)	Line	$F(\lambda)$ in 2006	$F(\lambda)$ in 2011	$I(\lambda)$ in 2006	$I(\lambda)$ in 2011
3726/29	[O II]	130.595 ± 0.345	126.8 ± 7.2	138.857 ± 2.801	163.0 ± 9.5
4101.73	B6	20.596 ± 0.031	18.4 ± 2.5	21.516 ± 0.395	21.6 ± 2.9
4340.46	B5	44.700 ± 0.067	45.8 ± 2.2	46.052 ± 0.579	50.9 ± 2.5
4363.21	[O III]	2.392 ± 0.004	4.1 ± 1.6	2.461 ± 0.030	4.6 ± 1.8
4958.91	[O III]	146.232 ± 0.237	150.8 ± 3.8	145.519 ± 0.380	148.0 ± 3.8
5754.64	[N II]	2.671 ± 0.006	3.9 ± 1.1	2.578 ± 0.038	3.3 ± 0.9
5875.60	He I	15.244 ± 0.115	18.1 ± 0.9	14.666 ± 0.262	15.2 ± 0.7
6300.30	[O I]	16.956 ± 0.021	22.5 ± 0.9	16.129 ± 0.339	17.7 ± 0.7
6312.10	[S III]	1.084 ± 0.003	1.6 ± 0.5	1.031 ± 0.022	1.2 ± 0.4
6363.78	[O I]	5.365 ± 0.09	8.3 ± 0.7	5.095 ± 0.111	6.5 ± 0.6
6548.04	[N II]	43.327 ± 0.054	60.9 ± 1.6	40.956 ± 0.967	46.5 ± 1.3
6583.46	[N II]	128.601 ± 0.168	190.2 ± 5.1	121.454 ± 2.915	144.6 ± 4.2
6678.15	He I	4.215 ± 0.007	5.6 ± 0.8	3.972 ± 0.099	4.2 ± 0.6
6716.44	[S II]	6.444 ± 0.010	11.3 ± 0.9	6.066 ± 0.154	8.5 ± 0.6
6730.81	[S II]	13.255 ± 0.021	21.6 ± 1.0	12.471 ± 0.319	16.1 ± 0.8
7065.18	He I	8.410 ± 0.101	10.3 ± 1.1	7.846 ± 0.247	7.4 ± 0.8
7135.80	[Ar III]	11.562 ± 0.018	17.3 ± 0.8	10.767 ± 0.322	12.3 ± 0.6

Note. $F(\lambda)$ and $I(\lambda)$ are normalized to the $F(\mathrm{H}\beta)$ and $I(\mathrm{H}\beta)$, where they equal 100, respectively.

Table 16
Adopting n_e and T_e for the Ionic Abundance Derivations

Ion	n_e (cm^{-3})	T_e (K)
N^0, O^0	1390	8470
S^+	5710	9280
C^{2+}(RL), O^{2+}(RL), N^{2+}(RL)	10,000	8090
He^+	10,000	8160
N^+, O^+, Cl^+, Fe^{2+}, Ar^+	17,520	9280
S^{2+}	21,990	8160
Ar^{2+}	21,990	8540
Ne^{2+}	22,720	8560
O^{2+}(CEL), S^{3+}, Ar^{3+}	22,750	9420
Ne^+	22,980	8540
Cl^{2+}	23,970	7490

Table 17
Twice Expansion Velocities of Hen3-1357

Ion	No. of sample	Emiss. type	IP (eV)	$2V_{exp}$ (km s^{-1})
H I	39	RL	13.60	14.78 ± 0.45
O I	5	RL	13.62	21.42 ± 1.13
N I	3	RL	14.53	18.44 ± 1.42
C II	2	RL	24.38	14.41 ± 1.51
He I	27	RL	24.59	16.28 ± 0.28
N II	3	RL	29.60	14.19 ± 1.78
O II	16	RL	35.12	16.43 ± 1.32
[C I]	1	CEL	0.00	18.06 ± 1.84
[N I]	2	CEL	0.00	17.52 ± 0.20
[O I]	3	CEL	0.00	14.86 ± 0.08
[Fe II]	3	CEL	7.87	15.25 ± 1.48
[S II]	4	CEL	10.36	14.21 ± 0.03
[Cl II]	2	CEL	12.97	16.94 ± 0.23
[O II]	6	CEL	13.62	13.73 ± 0.05
[N II]	4	CEL	14.53	14.37 ± 0.64
[Fe II]	8	CEL	16.18	17.97 ± 1.49
[S III]	3	CEL	23.33	13.53 ± 0.03
[Cl III]	3	CEL	23.81	14.17 ± 0.92
[Ar III]	3	CEL	27.63	13.09 ± 0.23
[O III]	3	CEL	35.12	14.19 ± 0.26
[Ar IV]	2	CEL	40.74	16.72 ± 0.91
[Ne III]	2	CEL	40.96	14.76 ± 0.04

Table 18
Comparison between the Observed and Model-predicted Line Fluxes, Band Fluxes, and Band Flux Densities

$\lambda_{lab.}$	Ion	I(obs) ($I(H\beta) = 100$)	I(model) ($I(H\beta) = 100$)
3697.2 Å	H I (B17)	1.923	1.146
3703.9 Å	H I (B16)	2.028	1.347
3712.0 Å	H I (B15)	2.384	1.606
3721.9 Å	H I (B14)	4.156	1.949
3726.0 Å	[O II]	101.210	133.154
3728.8 Å	[O II]	37.647	54.376
3734.4 Å	H I (B13)	3.026	3.039
3750.2 Å	H I (B12)	4.220	2.408
3770.6 Å	H I (B11)	4.353	3.930
3797.9 Å	H I (B10)	5.330	5.228
3819.6 Å	He I	1.142	1.228
3835.4 Å	H I (B9)	7.597	7.192
3867.5 Å	He I	0.147	0.107
3869.1 Å	[Ne III]	40.325	35.532
3889.1 Å	H I (B8)	15.997	10.316
3964.7 Å	He I	0.540	1.055
3967.8 Å	[Ne III]	10.000	10.709
3970.1 Å	H I (B7)	16.026	15.611
4026.2 Å	He I	1.532	2.229
4068.6 Å	[S II]	4.471	4.474
4075.0 Å	O II	0.197	0.134
4076.4 Å	[S II]	1.508	1.450
4101.7 Å	H I (B6, Hδ)	21.516	25.961
4120.8 Å	He I	0.177	0.209
4143.8 Å	He I	0.229	0.350
4267.2 Å	C II	0.103	0.126
4340.5 Å	H I (B5, Hγ)	46.052	46.863
4363.2 Å	[O III]	2.461	2.190
4387.9 Å	He I	0.439	0.596
4437.6 Å	He I	0.066	0.084
4471.5 Å	He I	4.628	4.853
4651.0 Å	O II	0.315	0.138
4658.1 Å	[Fe III]	0.111	0.222
4701.5 Å	[Fe III]	0.046	0.054
4711.4 Å	[Ar IV]	0.034	0.021
4713.2 Å	He I	0.668	0.662
4733.9 Å	[Fe III]	0.026	0.022
4740.2 Å	[Ar IV]	0.070	0.034
4754.7 Å	[Fe III]	0.029	0.025
4881.0 Å	[Fe III]	0.045	0.065
4921.9 Å	He I	1.214	1.293
4931.2 Å	[O III]	0.055	0.054
4958.9 Å	[O III]	145.519	131.766
4987.2 Å	[Fe III]	0.016	0.011
5015.7 Å	He I	2.161	2.655
5047.7 Å	He I	0.168	0.210
5191.8 Å	[Ar III]	0.064	0.137
5197.9 Å	[N I]	0.363	0.248
5200.3 Å	[N I]	0.228	0.152
5270.4 Å	[Fe III]	0.059	0.081
5517.7 Å	[Cl III]	0.117	0.191
5537.9 Å	[Cl III]	0.240	0.325
5577.3 Å	[O I]	0.219	0.142
5679.6 Å	N II	0.017	0.018
5754.6 Å	[N II]	2.578	2.946
5875.6 Å	He I	14.666	15.010
6300.3 Å	[O I]	16.129	7.661
6312.1 Å	[S III]	1.031	1.850
6363.8 Å	[O I]	5.095	2.443
6548.0 Å	[N II]	40.956	44.231
6583.5 Å	[N II]	121.454	130.527
6678.2 Å	He I	3.972	3.982
6716.4 Å	[S II]	6.066	3.861

Table 18
(Continued)

$\lambda_{lab.}$	Ion	I(obs) ($I(H\beta) = 100$)	I(model) ($I(H\beta) = 100$)
6730.8 Å	[S II]	12.471	7.635
7065.2 Å	He I	7.846	7.238
7135.8 Å	[Ar III]	10.767	19.209
7281.4 Å	He I	0.726	0.880
7319/20 Å	[O II]	17.485	17.826
7329/30 Å	[O II]	14.463	14.279
7751.1 Å	[Ar III]	2.630	4.635
8333.8 Å	H I (P24)	0.152	0.158
8345.6 Å	H I (P23)	0.188	0.175
8359.0 Å	H I (P22)	0.220	0.195
8361.7 Å	He I	0.082	0.098
8374.5 Å	H I (P21)	0.219	0.219
8392.4 Å	H I (P20)	0.252	0.248
8413.3 Å	H I (P19)	0.288	0.284
8434.0 Å	[Cl III]	0.008	0.013
8438.0 Å	H I (P18)	0.326	0.328
8467.3 Å	H I (P17)	0.378	0.383
8500.2 Å	[Cl III]	0.010	0.015
8502.5 Å	H I (P16)	0.450	0.454
8545.4 Å	H I (P15)	0.508	0.545
8578.7 Å	[Cl II]	0.304	0.200
8598.4 Å	H I (P14)	0.636	0.665
8617.0 Å	[Fe II]	0.042	0.031
8665.0 Å	H I (P13)	0.829	0.827
8727.1 Å	[C I]	0.014	0.019
8750.5 Å	H I (P12)	1.042	1.049
8891.9 Å	[Fe II]	0.016	0.010
9014.9 Å	H I (P10)	1.624	1.815
9052.0 Å	[Fe II]	0.011	0.007
9068.6 Å	[S III]	12.577	27.975
9123.6 Å	[Cl II]	0.103	0.052
5.92 μm	H I	0.740	0.464
6.99 μm	[Ar II]	7.435	1.015
9.01 μm	[Ar III]	12.993	17.582
10.51 μm	[S IV]	7.758	3.728
11.31 μm	H I	0.277	0.308
12.37 μm	H I	1.043	0.971
12.81 μm	[Ne II]	46.711	85.274
15.56 μm	[Ne III]	96.699	54.536
18.71 μm	[S III]	13.864	20.088
33.48 μm	[S III]	3.517	4.012
36.02 μm	[Ne III]	6.180	3.746

$\lambda_c(\Delta\lambda)$	Band	I(obs) ($I(H\beta) = 100$)	I(model) ($I(H\beta) = 100$)
3.56(0.68) μm	IRAC-1	17.926	14.099
4.51(0.86) μm	IRAC-2	20.919	13.128
5.74(1.26) μm	IRAC-3	12.618	10.021
7.93(2.53) μm	IRAC-4	48.754	45.385
9.22(4.10) μm	IRC-S9W	130.819	152.073
19.81(9.97) μm	IRC-L18W	1990.469	2062.191
65.0(20.17) μm	FIS-N60	327.889	327.959
90.0(39.90) μm	FIS-WS	283.292	219.030
140.0(54.74) μm	FIS-WL	32.158	25.831

$\lambda_c(\Delta\lambda)$	Band	I(obs) ($I(H\beta) = 100$)	I(model) ($I(H\beta) = 100$)
8.20(0.30) μm	IRS-1	1.613	2.279
9.55(0.10) μm	IRS-2	3.008	4.012
10.95(0.50) μm	IRS-3	21.065	29.324
14.95(0.50) μm	IRS-4	29.190	41.669
16.70(0.60) μm	IRS-5	98.078	95.574

Table 18
(Continued)

$\lambda_{\rm lab.}$	Ion	I(obs) ($I(\mathrm{H}\beta) = 100$)	I(model) ($I(\mathrm{H}\beta) = 100$)
18.10(0.60) μm	IRS-6	128.928	132.281
22.50(1.00) μm	IRS-7	215.444	217.328
29.50(1.00) μm	IRS-8	127.541	150.879
λ_c		F_ν(obs) (Jy)	F_ν(model) (Jy)
9.60 μm		0.097	0.110
17.60 μm		2.209	1.898
25.00 μm		3.718	3.746
27.00 μm		3.695	3.943
29.00 μm		3.790	4.060

Note. $\Delta\lambda$ indicates the bandwidth of each band. The predicted F_ν at IRAC-1/2/3/4 bands is 8.56, 1.01(+1), 8.62, and 3.70(+1) mJy, respectively. The F_ν at IRC-S9W/L18W bands is 1.03(+2) and 2.66(+3) mJy, respectively. The F_ν at FIS-N90/WS/WL is 2.25(+3), 1.46(+3), and 3.03(+2) mJy, respectively.

References

Arkhipova, V. P., Ikonnikova, N. P., Kniazev, A. Y., & Rajoelimanana, A. 2013, AstL, 39, 201
Asplund, M., Grevesse, N., Sauval, A. J., & Scott, P. 2009, ARA&A, 47, 481
Benjamin, R. A., Skillman, E. D., & Smits, D. P. 1999, ApJ, 514, 307
Bobrowsky, M. 1994, ApJL, 426, L47
Bobrowsky, M., Sahu, K. C., Parthasarathy, M., & García-Lario, P. 1998, Natur, 392, 469
Cahn, J. H., Kaler, J. B., & Stanghellini, L. 1992, A&AS, 94, 399
Cardelli, J. A., Clayton, G. C., & Mathis, J. S. 1989, ApJ, 345, 245
Cox, N. L. J., García-Hernández, D. A., García-Lario, P., & Manchado, A. 2011, AJ, 141, 111
DelgadoInglada, G., Morisset, C., & Stasińska, G. 2014, MNRAS, 440, 536
DelgadoInglada, G., & Rodríguez, M. 2014, ApJ, 784, 173
Dopita, M. A., & Meatheringham, S. J. 1991, ApJ, 377, 480
Fang, X., & Liu, X.-W. 2011, MNRAS, 415, 181
Fazio, G. G., Hora, J. L., Allen, L. E., et al. 2004, ApJS, 154, 10
Feibelman, W. A. 1995, ApJ, 443, 245
Ferland, G. J., Porter, R. L., van Hoof, P. A. M., et al. 2013, RMxAA, 49, 137
Frew, D. J. 2008, PhD thesis, Macquarie Univ.
Frew, D. J., Parker, Q. A., & Bojičić, I. S. 2016, MNRAS, 455, 1459
García-Hernández, D. A., & Górny, S. K. 2014, A&A, 567, A12
García-Hernández, D. A., Manchado, A., García-Lario, P., et al. 2002, A&A, 387, 955
Hamuy, M., Suntzeff, N. B., Heathcote, S. R., et al. 1994, PASP, 106, 566
Hamuy, M., Walker, A. R., Suntzeff, N. B., et al. 1992, PASP, 104, 533
Higdon, S. J. U., Devost, D., Higdon, J. L., et al. 2004, PASP, 116, 975
Houck, J. R., Roellig, T. L., van Cleve, J., et al. 2004, ApJS, 154, 18
Hubeny, I. 1988, CoPhC, 52, 103
Hyung, S., Aller, L. H., & Lee, W.-b. 2001, PASP, 113, 1559
Jones, D., Wesson, R., García-Rojas, J., Corradi, R. L. M., & Boffin, H. M. J. 2016, MNRAS, 455, 3263
Karakas, A., & Lattanzio, J. C. 2007, PASA, 24, 103
Karakas, A. I. 2010, MNRAS, 403, 1413
Kaufer, A., Stahl, O., Tubbesing, S., et al. 1999, Msngr, 95, 8
Kawada, M., Baba, H., Barthel, P. D., et al. 2007, PASJ, 59, S389
Kozok, J. R. 1985, A&AS, 62, 7
Liu, X.-W. 2006, in IAU Symp. 234, Planetary Nebulae in our Galaxy and Beyond, ed. M. J. Barlow & R. H. Méndez (Cambridge: Cambridge Univ. Press), 219
Liu, X.-W., Storey, P. J., Barlow, M. J., et al. 2000, MNRAS, 312, 585
Maciel, W. J., & Lago, L. G. 2005, RMxAA, 41, 383
Mallik, D. C. V., & Peimbert, M. 1988, RMxAA, 16, 111
Mathis, J. S., Rumpl, W., & Nordsieck, K. H. 1977, ApJ, 217, 425
Miranda, L. F., Guerrero, M. A., & Torrelles, J. M. 2001, MNRAS, 322, 195
Onaka, T., Matsuhara, H., Wada, T., et al. 2007, PASJ, 59, S401
Otsuka, M., Hyung, S., Lee, S.-J., Izumiura, H., & Tajitsu, A. 2009, ApJ, 705, 509
Otsuka, M., Hyung, S., & Tajitsu, A. 2015, ApJS, 217, 22
Otsuka, M., Tajitsu, A., Hyung, S., & Izumiura, H. 2010, ApJ, 723, 658
Otsuka, M., Tamura, S., Yadoumaru, Y., & Tajitsu, A. 2003, PASP, 115, 67
Parthasarathy, M. 2006, in IAU Symp. 234, Planetary Nebulae in our Galaxy and Beyond, ed. M. J. Barlow & R. H. Méndez (Cambridge: Cambridge Univ. Press), 79
Parthasarathy, M., García-Lario, P., de Martino, D., et al. 1995, A&A, 300, L25
Parthasarathy, M., Garcia-Lario, P., de Martino, D., Pottasch, S. R., & de Cordoba, S. F. 1997, in IAU Symp. 180, Planetary Nebulae, ed. H. J. Habing & H. J. G. L. M. Lamers (Cambridge: Cambridge Univ. Press), 123
Parthasarathy, M., García-Lario, P., Pottasch, S. R., et al. 1993, A&A, 267 L19
Parthasarathy, M., & Pottasch, S. R. 1989, A&A, 225, 521
Peimbert, M. 1967, ApJ, 150, 825
Peimbert, M., Peimbert, A., & Ruiz, M. T. 2000, ApJ, 541, 688
Perea-Calderón, J. V., García-Hernández, D. A., García-Lario, P., Szczerba, R., & Bobrowsky, M. 2009, A&A, 495, L5
Quireza, C., Rocha-Pinto, H. J., & Maciel, W. J. 2007, A&A, 475, 217
Reindl, N., Rauch, T., Miller Bertolami, M. M., Todt, H., & Werner, K. 2017, MNRAS, 464, L51
Reindl, N., Rauch, T., Parthasarathy, M., et al. 2014, A&A, 565, A40
Shaw, R. A., & Dufour, R. J. 1995, PASP, 107, 896
Stanghellini, L., García-Hernández, D. A., García-Lario, P., et al. 2012, ApJ, 753, 172
Stasińska, G., & Szczerba, R. 1999, A&A, 352, 297
Storey, P. J., & Hummer, D. G. 1995, MNRAS, 272, 41
Tajitsu, A., & Tamura, S. 1998, AJ, 115, 1989
Umana, G., Trigilio, C., Cerrigone, L., Buemi, C. S., & Leto, P. 2008, MNRAS, 386, 1404
van de Steene, G. C., & Zijlstra, A. A. 1995, A&A, 293, 541
Vassiliadis, E., & Wood, P. R. 1994, ApJS, 92, 125
Wang, W., & Liu, X.-W. 2007, MNRAS, 381, 669
Wesson, R., Liu, X.-W., & Barlow, M. J. 2005, MNRAS, 362, 424
Yamamura, I., Makiuti, S., Ikeda, N., et al. 2010, yCat, 2298
Zhang, C. Y. 1995, ApJS, 98, 659
Zhang, C. Y., & Kwok, S. 1991, A&A, 250, 179